
Reduced-Order Neural Operators: Learning Lagrangian Dynamics on Highly Sparse Graphs

Hrishikesh Viswanath
 Purdue University
 hviswan@purdue.edu

Yue Chang
 University of Toronto

Aleksey Panas
 University of Toronto

Julius Berner
 Nvidia

Peter Yichen Chen
 Massachusetts Institute of Technology

Aniket Bera
 Purdue University

Abstract

Simulating complex physical systems governed by Lagrangian dynamics often requires solving partial differential equations (PDEs) over high-resolution spatial domains, resulting in substantial computational costs. We present GIOROM (*Graph InfOrmed Reduced Order Modeling*), a data-driven discretization invariant framework for accelerating Lagrangian simulations through reduced-order modeling (ROM). Previous discretization invariant ROM approaches rely on PDE time-steppers for spatiotemporally evolving low-dimensional reduced-order latent states. Instead, we leverage a data-driven graph-based neural approximation of the PDE solution operator. This operator estimates point-wise function values from a sparse set of input observations, reducing reliance on known governing equations of numerical solvers. Order reduction is achieved by embedding these point-wise estimates within the reduced-order latent space using a learned kernel parameterization. This latent representation enables the reconstruction of the solution at arbitrary spatial query points by evolving latent variables over local neighborhoods on the solution manifold, using the kernel. Empirically, GIOROM achieves a $6.6 \times 32 \times$ reduction in input dimensionality while maintaining high-fidelity reconstructions across diverse Lagrangian regimes—including fluid flows, granular media, and elastoplastic dynamics. The resulting framework enables learnable, data-driven and discretization-invariant order-reduction with reduced reliance on analytical PDE formulations. Our code is at <https://github.com/HrishikeshVish/GIOROM>

1 Introduction

Various physical simulations involve simulating the spatio-temporal evolution of continuous fields governed by partial differential equations (PDEs) of the form

$$\mathcal{J}(\mathbf{f}, \nabla \mathbf{f}, \nabla^2 \mathbf{f}, \dots, \dot{\mathbf{f}}, \ddot{\mathbf{f}}, \dots) = \mathbf{0}, \quad (1)$$

$$\mathbf{f}(\mathbf{X}, t) : \Omega \times \mathcal{T} \rightarrow \mathbb{R}^d \quad (2)$$

where \mathbf{f} represents a multidimensional continuous vector field that depends on both space and time (e.g., position field, velocity field, etc.). The symbols ∇ and (\cdot) signify the spatial gradient and time derivative, respectively. Here, $\Omega \subset \mathbb{R}^d$ and $\mathcal{T} \subset \mathbb{R}$ denote the spatial and temporal domains, respectively. To solve such a system, we define the solution operator $\mathcal{J} : \mathbf{a} \rightarrow \mathbf{f}$, that maps a function of known observations $\mathbf{a} : \Omega' \times \mathcal{T}' \rightarrow \mathbb{R}^{d'}$ to \mathbf{f} , where we assume \mathbf{a} and \mathbf{f} to lie on Banach function spaces defined on bounded domains $D' \in \mathbb{R}^{d'}$ and $D \in \mathbb{R}^d$ respectively. We let \mathcal{M} denote the manifold of solutions over all parameters and time and d denotes the dimension (2 or 3).

To numerically solve the equation, the system is discretized spatially and temporally. Spatial discretization allows for the approximations $\mathbf{f}(\mathbf{X}, t) \approx \mathbf{f}_P(\mathbf{X}, t)$, and, $\mathbf{a}(\mathbf{X}, t) \approx \mathbf{a}_P(\mathbf{X}, t)$, where P represents the P -point spatial discretization in \mathbb{R}^d , transforming \mathbf{X} to a $(P \cdot d)$ -dimensional vector. Similarly, we introduce temporal samples $\{t_n\}_{n=1}^T$, so that, for a given sample $x \in \{x^i\}_{i=1}^P \in \mathbb{R}^{P \cdot d}$, we can compute the spatiotemporal evolution using a set of input state variables $\mathbf{a}_t = \mathbf{a}_P(x, t)$ to obtain the solution $\mathbf{f}_{t+1} = \mathbf{f}_P(x, t+1)$ at the next state. We omit double subscript for t for brevity. We focus on systems modeled by Lagrangian dynamics [109], in which the temporal evolution of interacting particles (represented as point-clouds) is governed by equations of motion derived from a Lagrangian functional encoding kinetic and potential energy contributions.

It has been shown that the computational cost of solving \mathcal{J} scales with the resolution P , making it computationally expensive to use full-order PDE solvers, which operate directly on $P \cdot d$ degrees of freedom [18, 19].

Reduced-order modeling (ROM) is used to approximate these dynamics on fewer degrees of freedom (e.g. $Q \ll P \cdot d$), reducing the computational cost [63]. This approach constrains the solution to evolve on a nonlinear low-dimensional manifold [18]. Such a low-dimension parameterization can be defined with a mapping, typically implemented as a neural network, $g : \mathbb{R}^Q \rightarrow \mathbb{R}^{P \cdot d}$, where $Q \ll P \cdot d$. This defines a map to a discrete field for every low dimensional latent vector $\hat{\mathbf{x}}(t) \in \mathbb{R}^Q$ such that $g_P(\hat{\mathbf{x}}) \mapsto (\mathbf{f}_t^1, \dots, \mathbf{f}_t^P)$ [17, 19]. For point-wise evaluations, $g(x^i, \hat{\mathbf{x}}_t) \approx \mathbf{f}(x^i, t) = \mathbf{f}_t^i$, with $\hat{\mathbf{x}}$ serving as a low-dimensional latent representation of the continuous field \mathbf{f} .

Discretization invariant ROM approaches [17, 19] construct the latent state $\hat{\mathbf{x}}_t$ from a known set of point-wise solution values $\phi = (\mathbf{f}_t^1, \dots, \mathbf{f}_t^P)$ through a projection map $\pi : \mathbb{R}^{P \cdot d} \rightarrow \mathbb{R}^Q$, often parameterized using PointNet-style encoders. Furthermore, temporal evolution, $\hat{\mathbf{x}}_t \mapsto \hat{\mathbf{x}}_{t+1}$, is implemented via explicit numerical time-stepping schemes with time gradients provided by the exact PDE. As a result, these methods depend on explicit access to both the PDE solution and the associated solver framework. Figure 1 illustrates this distinction by comparing particle trajectories in elastic deformation systems modeled using different ROM techniques.

In this paper, we propose a **data-driven discretization invariant** reduced-order modeling framework for Lagrangian systems. This is achieved by parameterizing the PDE solution operator \mathcal{J} with a data-driven neural parameterization $\phi_\Theta : a \rightarrow \hat{\mathbf{f}}$, trained from a small set of point-wise observations $\{\mathbf{a}_t^i, \mathbf{f}_t^i\}_{i=1}^r$ such that $\hat{\mathbf{f}}_t \approx \mathbf{f}_t$ and $\phi_\Theta \in \mathbb{R}^{r \cdot d}$, where $r \cdot d \ll P \cdot d$. We interpret ϕ_Θ to be a surrogate for the solution operator, with $\{x^i\}_{i=1}^r$ representing a form of hyperreduction of $(P \cdot d)$ -point samples in \mathbf{X} . The architecture for ϕ_Θ leverages graph interaction network [5, 89] to capture particle interaction dynamics.

Given a sparse set of function evaluations $\{\hat{\mathbf{f}}_t^i\}_{i=1}^r$ obtained using ϕ_Θ , our objective is to evaluate \mathbf{f} at arbitrary spatial locations through a low-dimensional latent representation. Instead of relying on trained projection (π) and decoder operators (g), we introduce a **neural kernel network** that directly maps sampled evaluations to a continuous spatial field. Such a mapping can be defined as $\kappa(x, \{\hat{\mathbf{f}}_t^i\}_{i=1}^r) \approx \mathbf{f}(x, t)$, where κ is the implicit kernel based manifold parameterization function.

Unlike global latent representations $\hat{\mathbf{x}}$ that embed the entire continuous field $\mathbf{f} \in \mathcal{M}$ into the latent vector, our kernel-based approach localizes evaluation around each query point. Specifically, the kernel restricts estimation to a *local region* within the manifold \mathcal{M} near the query location x^i , allowing us to reconstruct \mathbf{f}^i using the known neighboring samples obtained from ϕ_Θ . We show that this localized formulation improves accuracy in regions with complex geometric features such as fluid interfaces. In summary, we present,

Data-driven discretization-invariant reduced-order modeling framework: We present a neural framework for reduced-order modeling in Lagrangian systems. The framework enables spatiotemporal dynamics in the sampled space $\mathbb{R}^{r \cdot d}$, while evaluating at arbitrary spatial locations using a kernel-based low-dimensional manifold parameterization.

Robustness to sparse discretizations: Our proposed approach allows for hyperreduction of the samples in $\mathbb{R}^{P \cdot d}$. We achieve a reduction in input size ranging between $6.6\text{-}32\times$ compared to $(P \cdot d)$ -point discretization, while maintaining high-fidelity performance across diverse physical systems.

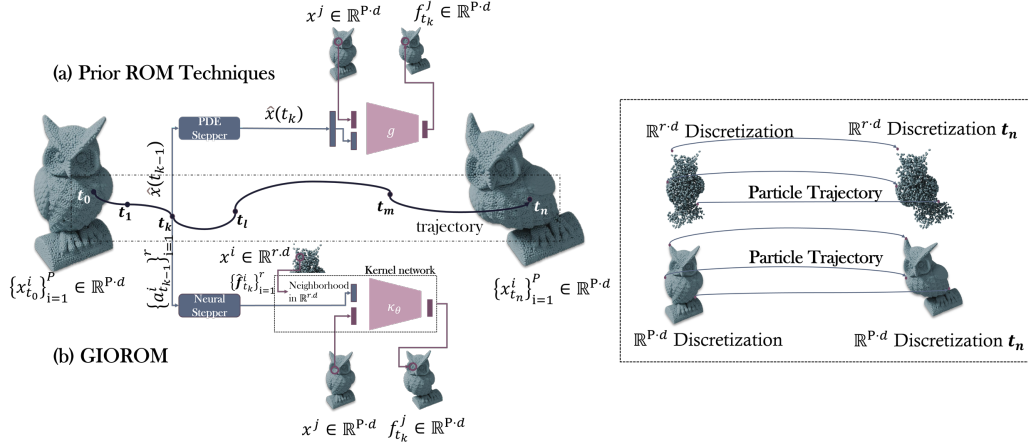


Figure 1: **Overview of GIOROM.** This figure illustrates the temporal evolution of Lagrangian systems using reduced-order modeling. (a) Prior discretization invariant methods evolve a global latent state \hat{x} using PDE time-steppers and reconstruct the full-field solution using neural decoders g . (b) In contrast, our approach employs a data-driven neural stepper to compute sparse field estimates $\{\hat{f}^i\}_{i=1}^r \in \mathbb{R}^{r \cdot d}$, which are then used by the kernel-ROM κ to parameterize the local solution manifold. f represents the deformation field depicted above.

Kernel based manifold parameterization: We propose a discretization invariant neural kernel network or kernel-ROM to estimate field values at arbitrary spatial locations, by restricting the solution to regions around the query point.

2 Related Works

Reduced-order models ROMs reduce computational cost by projecting high-dimensional systems onto low-dimensional manifolds [8, 35, 50, 75], often via sample selection [1]. Neural field-based ROMs [17, 19, 73, 102, 108] enable discretization-agnostic learning, supporting generalization across geometric discretizations, but are intrusive, requiring exact PDE formulation to time-step. Data-driven reduced-order modeling use deep-learning based techniques to achieve order-reduction [11, 30, 76], but they are not discretization invariant and require retraining to adapt to different discretizations. Kernel-based ROM techniques [36, 48, 70, 86, 88] leverage kernel methods such as Kernel-PCA or Kernel-POD, but they are discretization-dependent. Additional works are in appendix A.

Neural physics solvers Neural solvers have advanced simulations across fluid dynamics [32, 47, 67, 89, 93, 98], solid mechanics [16, 26, 43], climate modeling [74], and robotics [45, 72]. These models range from data-driven to physics-informed architectures [71, 85, 87, 94]. CNNs are effective on regular grids [4, 50, 68, 96], while GNNs generalize to irregular meshes, enabling applications in mesh-based dynamics [15, 23, 31, 79], Lagrangian systems [89], parametric PDEs [80], and rigid body physics [46]. However, GNNs scale poorly with graph size due to node-wise message passing. We aim to overcome this issue with spatial dimension reduction.

Neural operators Neural operators are a class of discretization-invariant models for learning mappings between infinite-dimensional function spaces. They have been applied to parametric PDEs [3, 27, 49, 52, 55, 58, 61, 62, 81, 82, 92, 100], fluid simulations [22, 78, 101], 3D physics [13, 34, 83, 103, 107], and even cross-domain tasks in biology, robotics, and vision [12, 21, 29, 59, 77, 84, 99]. Our work can be seen as bridging ROM with neural operators.

3 Definitions

Full-order model A full-order model evolves the solution over all degrees of freedom present in the spatial discretization scheme [37] (e.g., $P \cdot d$ in $\mathbb{R}^{P \cdot d}$ or $r \cdot d$ in $\mathbb{R}^{r \cdot d}$). These models do not perform any dimensionality reduction. They are therefore prohibitively slow when P is large. We

denote the P -point discretization of the spatial field \mathbf{X} by $\{x^j\}_{j=1}^P$, where x^j represents a particle in \mathbb{R}^d with negligible mass. Similarly, a sample set $\{x^i\}_{i=1}^r \subset \{x^j\}_{j=1}^P$ forms an $(r \cdot d)$ vector.

Reduced-order model A reduced-order model evolves the solution in reduced latent space \mathbb{R}^Q , $Q \ll P \cdot d$. Reduced-order techniques such as [19] leverage neural fields and projection-based ROM to infer the continuous spatial function at arbitrary spatial locations from the low-dimensional latents. In a similar vein, for an evaluation point x^i and its local spatial neighborhood $\tilde{x} = \mathcal{N}(x^i)$, we define our parameterization $\kappa(x^i, \phi_\Theta) \approx \mathbf{f}(x^i, t)$ as $\kappa(x^i, \phi_{\Theta, \tilde{x}}) \approx \mathbf{f}(x^i, t)$, for $x^i \in \mathbb{R}^d$, $\tilde{x} = \mathcal{N}(x^i)$, $\phi \in \mathbb{R}^{r \cdot d}$. We note here that κ parameterizes $\mathcal{M}(\mathbf{f})$ and $\phi_{\Theta, \tilde{x}} := \{\hat{\mathbf{f}}^j\}_{j \in \mathcal{N}(x^i)}$. We also note that $\hat{\mathbf{f}}$ has a temporal dependency, i.e. $\hat{\mathbf{f}}_t$ represents the evaluation at t . However, we omit the time subscript for brevity.

Time integration To compute temporal dynamics on these r -point spatial samples, we seek to evolve $\{\mathbf{f}_t^j\}_{j=1}^r \mapsto \{\mathbf{f}_{t+1}^j\}_{j=1}^r$. In the discrete setting, we leverage an explicit Euler time integrator [2] with step-size Δt ,

$$\mathbf{f}_{t+1}^j = \mathbf{f}_t^j + \Delta t \dot{\mathbf{f}}_t^j \quad (3)$$

$$\dot{\mathbf{f}}_{t+1}^j = \dot{\mathbf{f}}_t^j + \Delta t \ddot{\mathbf{f}}_t^j \quad (4)$$

If \mathbf{f}^j represents the position field, then, the one and only unknown in the equation above is the acceleration $\mathbf{A}_t^j = \ddot{\mathbf{f}}_t^j$, which is necessary for computing the velocity $\mathbf{V}_{t+1}^j = \dot{\mathbf{f}}_{t+1}^j$. We learn the acceleration field $\mathbf{A}_t^j := \ddot{\mathbf{f}}_t^j$ using the parameterization ϕ_Θ , which is then used in the explicit Euler update.

4 Method: Kernel-ROM

In this section, we discuss the mathematical formulation of the kernel-ROM framework, which enables the evaluation of the function \mathbf{f} at arbitrary query locations using a learned kernel function over a local neighborhood.

Let \mathbf{f} be the underlying spatiotemporal solution function, assumed to belong to Hilbert space \mathcal{H} of functions defined over $\Omega \in \mathbb{R}^d$ and $\mathcal{T} \in \mathbb{R}$. For a fixed $t \in \mathcal{T}$, we denote the spatial slice $\mathbf{f}_t : \Omega \rightarrow \mathbb{R}^d$. For brevity, we will omit the subscript t . The function \mathbf{f} is assumed to lie on a continuous, smooth solution manifold \mathcal{M} . We do not make assumptions regarding access to its closed form and instead are provided with a set of pointwise approximations $\{x^i, \hat{\mathbf{f}}^i\}_{i=1}^r$, where r is the number of sparse samples.

We seek to construct an estimator $\kappa(x, \hat{\mathbf{f}}) \approx \mathbf{f}(x, t)$ for any arbitrary $x \in \Omega$, where the approximation is achieved by an implicit kernel parameterization operating between a point in \mathbb{R}^d and the neighborhood in $\mathbb{R}^{r \cdot d}$, denoted as $\psi : \mathbb{R}^d \times \mathbb{R}^d \rightarrow \mathbb{R}^d$. Formally, this map $\kappa : \mathbb{R}^Q \rightarrow \mathbb{R}^{P \cdot d}$, is defined as $\kappa(x, \hat{\mathbf{f}}) := \sum_{y \in \mathcal{N}(x)} \psi_\theta(x, y) \hat{\mathbf{f}}(y, t)$, where ψ_θ is the kernel function parameterized by the neural network and the neighborhood $\mathcal{N}(x^i, \delta) = \{y \in \Omega : \|x^i - y\| \leq \delta\}$, where $\delta > 0$ is the neighborhood radius (training hyperparameter). Crucially, the estimator κ forms a continuous operator, with the domain and co-domain both being continuous and the estimator being discretization invariant.

In practice, we implement this as a discretization invariant kernel integral transform [56]. Leveraging ϕ_Θ (discussed in section 5) to obtain the estimates $\hat{\mathbf{f}}$, the complete kernel network parameterization can be given by:

$$\mathbf{f}(x, t) \approx \sum_{y \in \mathcal{N}(x)} \psi_\theta(x, y) \phi_\Theta(y, t), \quad x \in \{x^i\}_{i=1}^P, y \in \{x^j\}_{j=1}^r \quad (5)$$

where ψ_θ is the neural kernel parameterization and κ is analogous to the neural field in [19], $\phi_\Theta : a \rightarrow \hat{\mathbf{f}}$. We train the kernel network by minimizing the losses as follows

$$\mathcal{L}_\theta = \min_\theta \sum_{j=1}^P \sum_{t=1}^T \left\| \left(\sum_{\substack{y \in \mathcal{N}(x^j) \\ y \in \mathbb{R}^{r,d}}} \psi_\theta(x^j, y) \phi_\Theta(y, t) \right) - \mathbf{f}_t^j \right\|_2^2 \quad (6)$$

This estimator, while effectively serving as a neural field [106], differs from the neural fields proposed in [17, 19] in two ways - (1) We restrict the kernel to local neighborhoods of the evaluation point within the solution manifold to better capture fluid interfaces; (2) The framework is discretization invariant to the function in $(r.d)$ -point discretization. The second follows from the discretization invariant properties of this kernel formulation, as discussed in [56]. However, the [19] framework relies on discretization dependent projection operator π to obtain $\hat{\mathbf{x}}$.

5 Method: Time-stepping on sparse graphs

We make a deviation in this section to focus on obtaining the sample set $\{x^i, \hat{\mathbf{f}}^i\}_{i=1}^r$, which is done using ϕ_Θ . With $r \ll P$, we only require evaluating the *full-order dynamics* on a sparse set of points, achieving computational speedups. We leverage graph interaction networks [5, 89] to model ϕ_Θ , due to their strong expressivity in modeling particle interaction dynamics.

5.1 Step 1: Graph representation

We consider a reduced set of material points $\{x^i\}_{i=1}^r$, with $r \ll P$, for which we seek full-order evaluations without assuming a specific sampling scheme. Importantly, we do not train ϕ_Θ for a fixed r . The model ϕ_Θ is trained on coarse discretizations $\{x^i, a^i, \mathbf{f}^i\}_{i=1}^r$, where $|\mathbf{V}| \ll P \cdot d$, defined on a radius graph $\mathbf{G} = (\mathbf{V}, \mathbf{E})$. Here, \mathbf{V} denotes particles and \mathbf{E} contains undirected edges between nodes within radius ρ_s , i.e., $(x, y) \in \mathbf{E} \iff d(x, y) \leq \rho_s$. The edges represent particle interactions.

For a subgraph $\mathbf{H} = (v, \varepsilon)$, defined over $v \subseteq \mathbf{V}$ with edges induced by radius ρ_r , we view \mathbf{G} and \mathbf{H} as discrete approximations of an underlying continuous manifold $\mathcal{C} \subset \mathbb{R}^d$ [14, 44]. We observe that for reasonable sizes of \mathbf{H} , we can tune the radius ρ_r and enforce that for $x^i \in \mathbf{V} \cap v$, $\phi_{\Theta, \mathbf{H}}(x^i, t) \approx \phi_{\Theta, \mathbf{G}}(x^i, t) := \hat{\mathbf{f}}^i$, where $\phi_{\Theta, \mathbf{G}}$ represents the model operating on graph \mathbf{G} . This is achieved by enforcing a discrete neural operator behavior within the GNN architecture. We require tuning of ρ_r as fewer nodes alter local neighborhoods, which can disrupt message passing [24, 25].

5.2 Step 2: Heuristic for graph construction

For a subgraph \mathbf{H} defined on $v \subseteq \mathbf{V}$, we require the connectivity radius $\rho_r \geq \rho_s$ to preserve paths between originally connected nodes, even after subsampling; r is chosen to optimize kernel-ROM performance/cost tradeoff, and consequently, ρ_r is tuned at inference to trade off accuracy and speed.

We use mean aggregation in message passing to ensure consistent node features across discretizations. This is shown to behave like a Monte Carlo approximation of kernel integrals, enabling the GNN to function as a neural operator under suitable graph construction [54].

Prior sampling-based ROM approaches rely on stochastic, residual-guided strategies to select sample sets [19]. In contrast, we adopt simple sampling methods such as random or farthest-point selection. To ensure invariance to the sampling ratio for $r := |v|/|\mathbf{V}|$, we construct l random subgraphs per input domain to evaluate during training. This can be seen as a Nyström-type approximation, reducing variance and improving generalization across discretizations.

Empirically, we find that overly small $|v|$ degrades accuracy even with large ρ_r , implying a lower bound on r to retain spatial structure. This threshold guides inference-time subgraph construction (appendix J). Conversely, excessive ρ_r introduces redundant edges and deteriorates performance due to loss of locality.

5.3 Step 3: Spatio-temporal time-stepping

Equipped with our data structure \mathbf{H} , we now discuss the architecture of ϕ_Θ that enables the mapping $a_t^j \rightarrow \hat{\mathbf{f}}_{t+1}^j$. We define a^j and \mathbf{f}^j to be point-wise function values defined on the node set $v \in \mathbb{R}^{r \cdot d}$.

Following [5, 23, 89], we leverage the GNN-based Interaction Network (IN) that follows an encode-process-decode framework. However, this architecture incurs computational bottlenecks associated with stacked GNN layers. To improve the computational speed and to learn global spatial information, we replace the process part of the framework with a Neural Operator Transformer (NOT), as proposed in [33]. The NOT can be viewed as a sequence of global GNN layers, which operate over a latent node embedding generated by the Interaction Network encoder (IN), which is still necessary to capture the interaction dynamics of Lagrangian systems. Our formulation can then be defined as

$$\phi_\Theta := IN^{dec, \mathbf{H}} \circ NOT^{process} \circ IN^{enc, \mathbf{H}} \quad (7)$$

Where *enc* and *dec* denote the encoder and decoder, which operate on the graph \mathbf{H} . The NOT however operates only on the latent embeddings. The input for the model is the velocity sequence v defined over a time window w . Formally, $a_t^j = \mathbf{v}_{t-w:t}^j, \forall j \in \mathbb{R}^{r \cdot d}$. The output is then given as $\hat{\mathbf{f}}_t^j = \mathbf{a}_t^j$, where \mathbf{a} is the pointwise acceleration defined on v . We obtain $\hat{\mathbf{f}}_{t+1}^j$ by Euler integration. The model is trained following [89] with data-driven losses as follows

$$\mathcal{L}_\Theta = \min_\Theta \sum_j \|\phi_\Theta(a_t^j) - \ddot{\mathbf{f}}_t^j\|_2^2 \quad (8)$$

Additional training details and hyperparameter information is provided in appendix E and appendix G

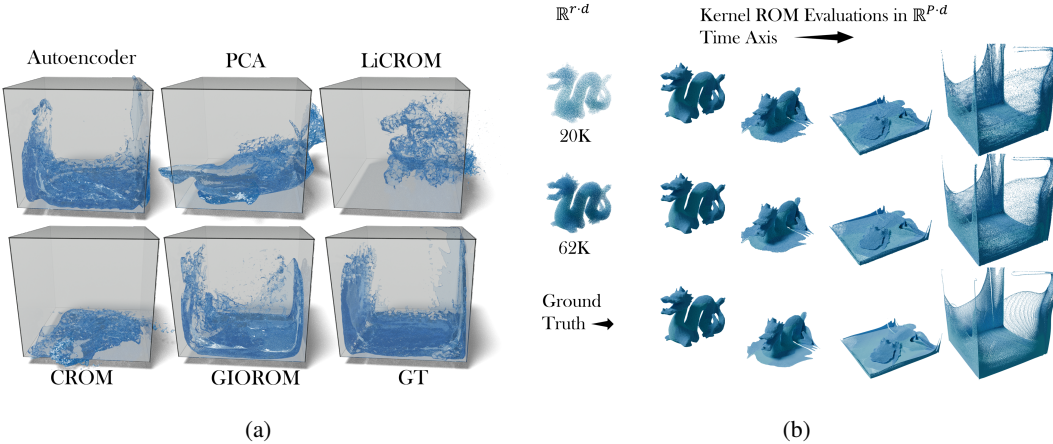


Figure 2: (a) **Comparison of reduced-order modeling (ROM) techniques on fluid-in-container simulations:** The visualization reveals that the baseline models PCA (rollout MSE: 0.083), Autoencoder (0.091), LiCROM (0.033), and CROM (0.079), exhibit noticeable deviation from the true fluid boundaries, including overshooting beyond the container. GIOROM maintains physical fidelity with a lower rollout MSE of 0.0091. (b) **Demonstration of discretization convergence of kernel-ROM on high-resolution particle systems:** Contrasting the behavior of the kernel-ROM on a large-scale simulation containing approximately 2 million particles, discretized as voxelized grids. Using randomly sampled $(r \cdot d)$ -points of 62K and 20K particles (sampling percentages of 3% and 1%), the rollout MSEs are 0.0097 and 0.0088, respectively. These results indicate discretization convergence of κ under resolution refinement.

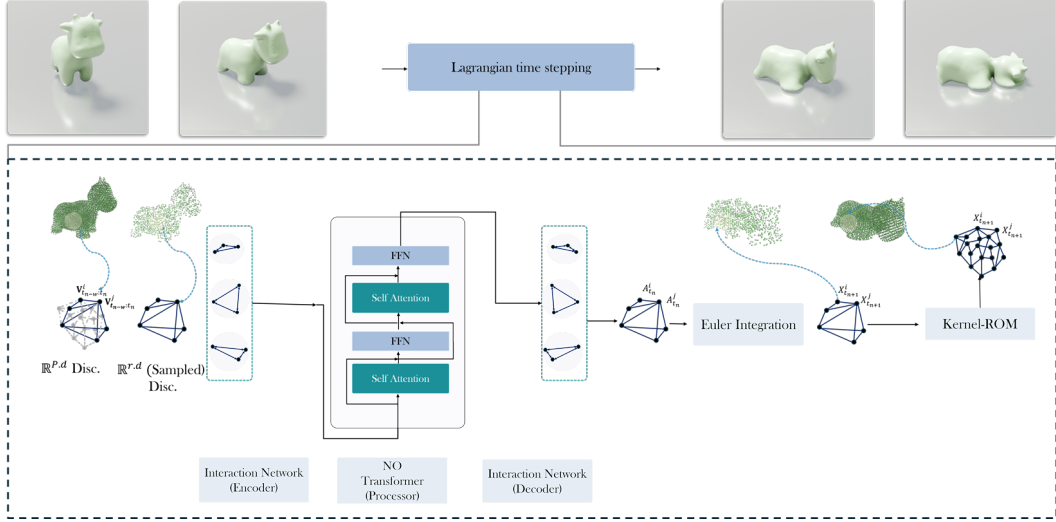


Figure 3: **The overall architecture of GIOROM.** The neural time-stepper ϕ_Θ (Encoder-Processor-Decoder) predicts the acceleration of a Lagrangian system \mathbf{A}_t at time t from the past w velocity instances $\mathbf{V}_{t-w:t}$. From the predicted accelerations, we leverage standard Euler integration to obtain the predicted positions. The rightmost kernel-ROM is used to efficiently evaluate the deformation field at arbitrary locations. This is summarized in the flow diagram fig. 6

Table 1: This table showcases the performance of GIOROM on several physical systems. These results are computed on $\mathbb{R}^{P \cdot d}$.

PHYSICAL SYSTEM	DURATION ($5e^{-3}$ s)	EVAL PTS FOR κ IN $\mathbb{R}^{P \cdot d}$	INPUT GRAPH SIZE $\mathbb{R}^{r \cdot d}$	SCALE	ONE STEP-MSE ($\times e^{-9}$)	ROLLOUT MSE ($\times e^{-3}$)
WATER-3D	1000	55k	1.7k	32 \times	5.23	0.386
WATER-2D	1000	1k	0.12k	8.3 \times	0.524	6.7
SAND-3D	400	32k	1k	32 \times	4.87	0.0025
SAND-2D	320	2k	0.3k	6.6 \times	8.5	1.34
GOOP-2D	400	1.9k	0.2k	9.5 \times	1.31	0.94
PLASTICINE	320	5k	1.1k	4.5 \times	0.974	0.5
ELASTICITY	120	78k	2.6k	30 \times	0.507	0.2
MULTI-MATERIAL 2D	1000	2k	0.25k	8 \times	2.3	9.43

6 Experiments

6.1 Dataset

Our dataset consists of four 3D physical systems - Newtonian fluids (Water), Drucker-Prager elasto-plasticity (Sand), von Mises yield (Plasticine) and purely Elastic deformations. Unless otherwise noted, we assume the discretization to be point clouds.

We used the nclaw simulator [64] to generate 100 trajectories for each of these systems with random initial velocity conditions and a fixed boundary $[0, 1], [0, 1], [0, 1]$, with a free-slip boundary condition. The Δt between consecutive time frames is $5e^{-3}$ s. We additionally used datasets provided by [89] - WaterDrop, Water-3D, Sand-3D, Sand, Goop and MultiMaterial. Additional training details and model hyperparameters can be found in Appendix E.2.

6.2 Results

Performance on different physical systems We evaluate GIOROM on a held-out validation set of unseen trajectories from multiple physical systems. Table 1 reports mean-squared error (MSE) for both single-step predictions and long-horizon rollouts, where the sample evaluations $\{x^i, \hat{f}^i\}_{i=1}^r$ produced by ϕ_Θ are used by the kernel network to compute high-resolution evaluations in $\mathbb{R}^{P \cdot d}$.

These are compared against ground-truth trajectories at the same resolution. Qualitative results in Figure 8 illustrate rollout fidelity, with Figure 5 demonstrating stability until equilibrium. Additional results and discussions are provided in appendix H and appendix J.

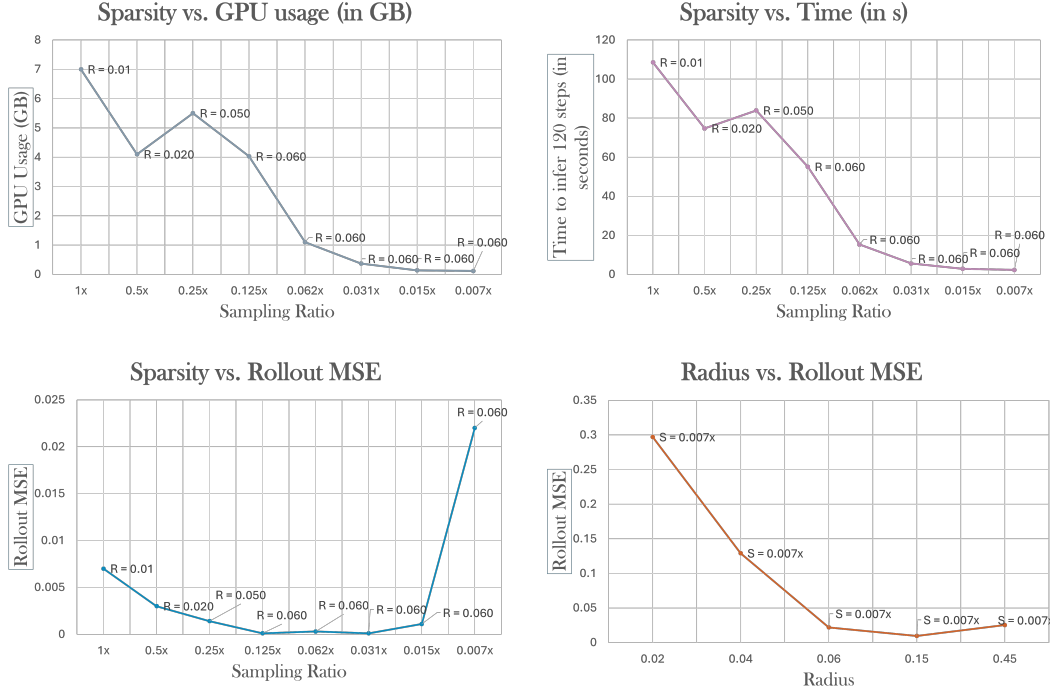


Figure 4: **Effect of sparsity on rollout error (Elasticity dataset, 78K particles).** Plots show performance of ϕ_Θ across varying sparsity levels, expressed as a fraction of the full system. GPU usage and computation time include pre-processing overhead for graph construction at each rollout step. Top-left plot reports peak GPU usage across graph sizes (R =radius, S =sample ratio); top-right shows net computation time for a rollout as a function of sparsity at fixed radius. Bottom-left plot reports rollout MSE, showing that performance remains stable ($\sim 1e-4$) for sparsity levels $0.125\times$, $0.062\times$, and $0.031\times$. Below this, performance degrades due to oversparsification. Bottom-right plot shows that for high sparsification ($0.007\times$), increasing the graph radius beyond 0.15 does not improve performance.

Table 2: This table highlights resolution and discretization generalization of ϕ_Θ in different settings of the Elasticity dataset.

SETTING	AVERAGE NUM. POINTS	SCALE W.R.T TRAINING DATA	ONE-STEP MSE ($\times 10^{-9}$)	ROLLOUT MSE ($\times 10^{-3}$)
SIMILAR DISC.	2.5k	1.25	0.8	0.2
LOWER RES.	1k	0.5	1.9	0.5
LOWER RES.	0.5k	0.25	2.34	0.6
HIGHER RES.	5k	2	0.319	0.7
HIGHER RES.	10k	4	0.88	0.9
INFERENCE ON $\mathbb{R}^{P \cdot d}$	78k	52	94.4	2

Robustness to sparse sample size r We evaluate the robustness of ϕ_Θ to varying sampling resolutions r on the elasticity dataset (full-order: 78K particles), as shown in Table 2. The first row reports performance on validation graphs closely matching training resolution ($\sim 1.2\times$ particle count). We assess generalization at coarser ($0.25\times$, $0.5\times$) and finer ($2\times$, $4\times$) resolutions, with trends shown in fig. 4. Inference at $(P \cdot d)$ -point discretization shows minor degradation, underscoring the scalability limitations of GNNs and the need for reduced-order models.

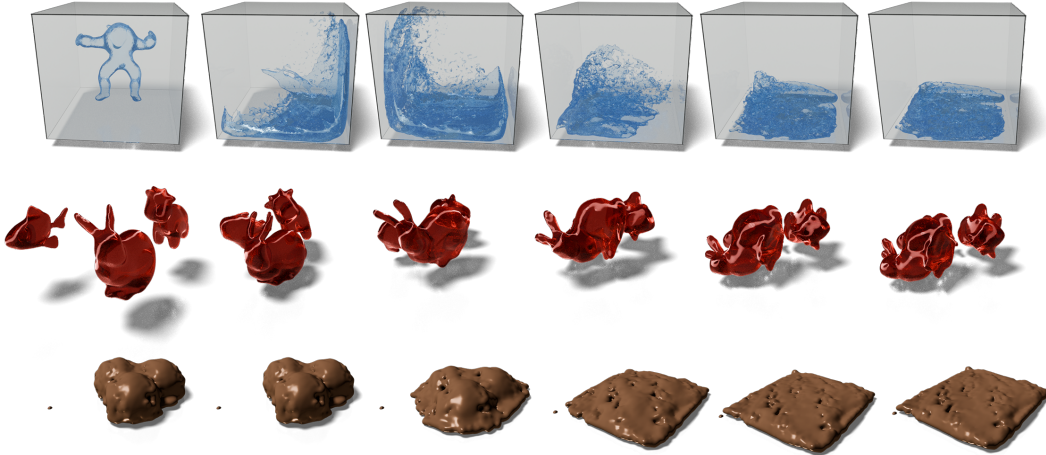


Figure 5: Rollout trajectories for three physical systems evaluated until equilibrium. **(Top)** Water simulation with high dynamism, rolled out for 1000 time steps over 55K particles; rollout MSE: 1.1×10^{-2} . **(Middle)** Elastic collisions (Jelly) over 500 time steps with 84K particles; rollout MSE: 6.4×10^{-5} . **(Bottom)** Phase transition in plasticine-like material (Chocolate) over 2000 time steps with 24K particles; rollout MSE: 3.2×10^{-4} .

6.3 Baselines

ROM baselines We evaluate our proposed kernel-ROM against reduced-order models. We evaluate the prior models on highly dynamic water simulations with neighborhood changes, a scenario that is difficult for ROM techniques to model. We discuss the results in fig. 2a. The baselines we compared include (1) PCA (Principal Component Analysis), also known as POD (Proper Orthogonal Decomposition), (2) Autoencoders [50], (3) LICROM [17], and (4) CROM [19].

7 Discussions and Conclusion

Computational Efficiency We evaluated the relationship between graph sparsity and both computational speed and memory consumption. As shown in fig. 4, increasing sparsity yields significant performance gains without compromising accuracy, up to a reduction factor of $0.031\times$, even for systems with approximately 78k particles.

Robustness to Sparsity Variations We tested the model under varying sparsity levels with appropriate graph structure. The model remains stable under super-sampling; however, performance degrades when sparsity exceeds the $0.031\times$ threshold. These results, visualized in fig. 4, indicate a practical lower bound on sample density. We provide more discussions in appendix J.

Conclusion We show that our reduced-order modeling framework for learning Lagrangian dynamics on sparse inputs achieves computational improvements over existing neural solvers (table 5) while preserving high simulation fidelity across diverse physical systems, outperforming traditional ROM approaches, particularly, on dynamic fluid simulations. The end-to-end data-driven approach can open doors to incorporating model-order reduction to simulations generated by generative models, with no PDE priors.

Nonetheless, several limitations remain. GIOROM, like other learning-based ROMs, exhibits reduced performance under extreme out-of-distribution conditions [19, 54] and extreme sparsifications (appendix J.2). Furthermore, while currently designed for continuous systems, future work may extend GIOROM to explicitly address discontinuities [6, 28] and unbounded flows. GIOROM is flexible to any choice of neural time-stepper, however, it faces the limitations imposed by the choice of the time-stepper. While we currently only leverage Euler integration schemes, studying the impacts of higher-order methods, such as Runge-Kutta 4th order on accuracy or stability of ROM is an exciting

future direction. We also restrict our problem setups to consistent time-discretizations. Understanding the behavior of neural time-steppers on varying time discretization is another consideration for future work.

Acknowledgment

We thank Aleksey Panas and Jiahao Xu from the DGP Lab at University of Toronto for rendering the simulations presented in this paper. We thank Shreyas Samaga and Mark He from Purdue University for their inputs on graph learning.

References

- [1] S. S. An, T. Kim, and D. L. James. Optimizing cubature for efficient integration of subspace deformations. *ACM transactions on graphics (TOG)*, 27(5):1–10, 2008.
- [2] U. M. Ascher and L. R. Petzold. *Computer methods for ordinary differential equations and differential-algebraic equations*. SIAM, 1998.
- [3] K. Azizzadenesheli, N. Kovachki, Z. Li, M. Liu-Schiaffini, J. Kossaifi, and A. Anandkumar. Neural operators for accelerating scientific simulations and design. *Nature Reviews Physics*, pages 1–9, 2024.
- [4] F. Bamer, D. Thaler, M. Stoffel, and B. Markert. A monte carlo simulation approach in non-linear structural dynamics using convolutional neural networks. *Frontiers in Built Environment*, 7, 2021.
- [5] P. Battaglia, R. Pascanu, M. Lai, D. Jimenez Rezende, et al. Interaction networks for learning about objects, relations and physics. *Advances in neural information processing systems*, 29, 2016.
- [6] Y. Belhe, M. Gharbi, M. Fisher, I. Georgiev, R. Ramamoorthi, and T.-M. Li. Discontinuity-aware 2d neural fields. *ACM Transactions on Graphics (TOG)*, 42(6):1–11, 2023.
- [7] M. Belkin and P. Niyogi. Laplacian eigenmaps for dimensionality reduction and data representation. *Neural computation*, 15(6):1373–1396, 2003.
- [8] G. Berkooz, P. Holmes, and J. L. Lumley. The proper orthogonal decomposition in the analysis of turbulent flows. *Annual review of fluid mechanics*, 25(1):539–575, 1993.
- [9] A. Berlinet and C. Thomas-Agnan. *Reproducing kernel Hilbert spaces in probability and statistics*. Springer Science & Business Media, 2011.
- [10] T. Berry and T. Sauer. Local kernels and the geometric structure of data. *Applied and Computational Harmonic Analysis*, 40(3):439–469, 2016.
- [11] L. Besabe, M. Girfoglio, A. Quaini, and G. Rozza. Data-driven reduced order modeling of a two-layer quasi-geostrophic ocean model. *Results in Engineering*, 25:103691, 2025.
- [12] R. Bhaskara, H. Viswanath, and A. Bera. Trajectory prediction for robot navigation using flow-guided markov neural operator. *arXiv preprint arXiv:2309.09137*, 2023.
- [13] B. Bonev, T. Kurth, C. Hundt, J. Pathak, M. Baust, K. Kashinath, and A. Anandkumar. Spherical fourier neural operators: Learning stable dynamics on the sphere. In *International conference on machine learning*, pages 2806–2823. PMLR, 2023.
- [14] D. Burago, S. Ivanov, and Y. Kurylev. A graph discretization of the laplace–beltrami operator. *Journal of Spectral Theory*, 4(4):675–714, 2015.
- [15] Y. Cao, M. Chai, M. Li, and C. Jiang. Efficient learning of mesh-based physical simulation with bsms-gnn. *arXiv preprint arXiv:2210.02573*, 2022.
- [16] G. Capuano and J. J. Rimoli. Smart finite elements: A novel machine learning application. *Computer Methods in Applied Mechanics and Engineering*, 345:363–381, 2019.
- [17] Y. Chang, P. Y. Chen, Z. Wang, M. M. Chiaramonte, K. Carlberg, and E. Grinspun. Licrom: Linear-subspace continuous reduced order modeling with neural fields. In *SIGGRAPH Asia 2023 Conference Papers*, SA ’23, New York, NY, USA, 2023. Association for Computing Machinery.

- [18] P. Y. Chen, M. Chiaramonte, E. Grinspun, and K. Carlberg. Model reduction for the material point method via learning the deformation map and its spatial-temporal gradients. *URL: <http://arxiv.org/abs/2109.12390 v1>*, 2021.
- [19] P. Y. Chen, J. Xiang, D. H. Cho, Y. Chang, G. A. Pershing, H. T. Maia, M. M. Chiaramonte, K. T. Carlberg, and E. Grinspun. CROM: Continuous reduced-order modeling of PDEs using implicit neural representations. In *The Eleventh International Conference on Learning Representations*, 2023.
- [20] R. R. Coifman and S. Lafon. Diffusion maps. *Applied and computational harmonic analysis*, 21(1):5–30, 2006.
- [21] G. Dharuman, L. Ward, H. Ma, P. V. Setty, O. Gokdemir, S. Foreman, M. Emani, K. Hippe, A. Brace, K. Keipert, et al. Protein generation via genome-scale language models with bio-physical scoring. In *Proceedings of the SC’23 Workshops of The International Conference on High Performance Computing, Network, Storage, and Analysis*, pages 95–101, 2023.
- [22] P. C. Di Leoni, L. Lu, C. Meneveau, G. E. Karniadakis, and T. A. Zaki. Neural operator prediction of linear instability waves in high-speed boundary layers. *Journal of Computational Physics*, 474:111793, 2023.
- [23] M. Fortunato, T. Pfaff, P. Wirnsberger, A. Pritzel, and P. Battaglia. Multiscale meshgraphnets. *arXiv preprint arXiv:2210.00612*, 2022.
- [24] Z. Gao and E. Isufi. Learning stable graph neural networks via spectral regularization. In *2022 56th Asilomar Conference on Signals, Systems, and Computers*, pages 01–05. IEEE, 2022.
- [25] V. Garg, S. Jegelka, and T. Jaakkola. Generalization and representational limits of graph neural networks. In *International conference on machine learning*, pages 3419–3430. PMLR, 2020.
- [26] A. R. Geist and S. Trimpe. Structured learning of rigid-body dynamics: A survey and unified view from a robotics perspective. *GAMM-Mitteilungen*, 44(2):e202100009, 2021.
- [27] S. Goswami, A. Bora, Y. Yu, and G. E. Karniadakis. Physics-informed deep neural operator networks. In *Machine Learning in Modeling and Simulation: Methods and Applications*, pages 219–254. Springer, 2023.
- [28] S. Goswami, M. Yin, Y. Yu, and G. E. Karniadakis. A physics-informed variational deeponet for predicting crack path in quasi-brittle materials. *Computer Methods in Applied Mechanics and Engineering*, 391:114587, 2022.
- [29] J. Guibas, M. Mardani, Z. Li, A. Tao, A. Anandkumar, and B. Catanzaro. Adaptive fourier neural operators: Efficient token mixers for transformers. *arXiv preprint arXiv:2111.13587*, 2021.
- [30] M. Guo and J. S. Hesthaven. Data-driven reduced order modeling for time-dependent problems. *Computer methods in applied mechanics and engineering*, 345:75–99, 2019.
- [31] X. Han, H. Gao, T. Pfaff, J.-X. Wang, and L.-P. Liu. Predicting physics in mesh-reduced space with temporal attention. *arXiv preprint arXiv:2201.09113*, 2022.
- [32] Z. Hao, C. Su, S. Liu, J. Berner, C. Ying, H. Su, A. Anandkumar, J. Song, and J. Zhu. DPOT: Auto-regressive denoising operator transformer for large-scale pde pre-training. *arXiv preprint arXiv:2403.03542*, 2024.
- [33] Z. Hao, Z. Wang, H. Su, C. Ying, Y. Dong, S. Liu, Z. Cheng, J. Song, and J. Zhu. Gnot: A general neural operator transformer for operator learning. In *International Conference on Machine Learning*, pages 12556–12569. PMLR, 2023.
- [34] J. He, S. Koric, D. Abueidda, A. Najafi, and I. Jasiuk. Geom-deeponet: A point-cloud-based deep operator network for field predictions on 3d parameterized geometries. *arXiv preprint arXiv:2403.14788*, 2024.
- [35] P. Holmes, J. L. Lumley, G. Berkooz, and C. W. Rowley. *Turbulence, coherent structures, dynamical systems and symmetry*. Cambridge university press, 2012.
- [36] P. Honeine. Online kernel principal component analysis: A reduced-order model. *IEEE transactions on pattern analysis and machine intelligence*, 34(9):1814–1826, 2011.
- [37] T. J. Hughes. *The finite element method: linear static and dynamic finite element analysis*. Courier Corporation, 2012.

[38] A. J. Izenman. Introduction to manifold learning. *Wiley Interdisciplinary Reviews: Computational Statistics*, 4(5):439–446, 2012.

[39] S. Janny, M. Nadri, J. Digne, and C. Wolf. Space and time continuous physics simulation from partial observations. In *International Conference on Learning Representation*, Vienna, Austria, May 2024.

[40] J. Jeon, J. Lee, R. Vinuesa, and S. J. Kim. Residual-based physics-informed transfer learning: A hybrid method for accelerating long-term cfd simulations via deep learning. *International Journal of Heat and Mass Transfer*, 220:124900, 2024.

[41] C. Jiang, C. Schroeder, J. Teran, A. Stomakhin, and A. Selle. The material point method for simulating continuum materials. *ACM SIGGRAPH 2016 Courses*, pages 1–52, 2016.

[42] R. Jiang, P. Y. Lu, E. Orlova, and R. Willett. Training neural operators to preserve invariant measures of chaotic attractors. *Advances in Neural Information Processing Systems*, 36, 2024.

[43] H. Jin, E. Zhang, and H. D. Espinosa. Recent advances and applications of machine learning in experimental solid mechanics: A review. *Applied Mechanics Reviews*, 75(6):061001, 2023.

[44] Y. Jin, A. Loukas, and J. JaJa. Graph coarsening with preserved spectral properties. In *International Conference on Artificial Intelligence and Statistics*, pages 4452–4462. PMLR, 2020.

[45] B. Kaczmarski, A. Goriely, E. Kuhl, and D. E. Moulton. A simulation tool for physics-informed control of biomimetic soft robotic arms. *IEEE Robotics and Automation Letters*, 8(2):936–943, 2023.

[46] J. Kneifl, J. Fehr, S. L. Brunton, and J. N. Kutz. Multi-hierarchical surrogate learning for structural dynamics of automotive crashworthiness using graph convolutional neural networks. *arXiv preprint arXiv:2402.09234*, 2024.

[47] D. Kochkov, J. A. Smith, A. Alieva, Q. Wang, M. P. Brenner, and S. Hoyer. Machine learning–accelerated computational fluid dynamics. *Proceedings of the National Academy of Sciences*, 118(21):e2101784118, 2021.

[48] J. Kou and W. Zhang. Multi-kernel neural networks for nonlinear unsteady aerodynamic reduced-order modeling. *Aerospace Science and Technology*, 67:309–326, 2017.

[49] N. Kovachki, Z. Li, B. Liu, K. Azizzadenesheli, K. Bhattacharya, A. Stuart, and A. Anandkumar. Neural operator: Learning maps between function spaces with applications to pdes. *Journal of Machine Learning Research*, 24(89):1–97, 2023.

[50] K. Lee and K. T. Carlberg. Model reduction of dynamical systems on nonlinear manifolds using deep convolutional autoencoders. *Journal of Computational Physics*, 404:108973, 2020.

[51] S. Lee and T. Oh. Inducing point operator transformer: A flexible and scalable architecture for solving pdes. In *Proceedings of the AAAI Conference on Artificial Intelligence*, volume 38, pages 153–161, 2024.

[52] Z. Li, D. Z. Huang, B. Liu, and A. Anandkumar. Fourier neural operator with learned deformations for pdes on general geometries. *Journal of Machine Learning Research*, 24(388):1–26, 2023.

[53] Z. Li, N. Kovachki, K. Azizzadenesheli, B. Liu, K. Bhattacharya, A. Stuart, and A. Anandkumar. Fourier neural operator for parametric partial differential equations. *arXiv preprint arXiv:2010.08895*, 2020.

[54] Z. Li, N. Kovachki, K. Azizzadenesheli, B. Liu, K. Bhattacharya, A. Stuart, and A. Anandkumar. Neural operator: Graph kernel network for partial differential equations. *arXiv preprint arXiv:2003.03485*, 2020.

[55] Z. Li, N. Kovachki, K. Azizzadenesheli, B. Liu, A. Stuart, K. Bhattacharya, and A. Anandkumar. Multipole graph neural operator for parametric partial differential equations. *Advances in Neural Information Processing Systems*, 33:6755–6766, 2020.

[56] Z. Li, N. Kovachki, C. Choy, B. Li, J. Kossaifi, S. Otta, M. A. Nabian, M. Stadler, C. Hundt, K. Azizzadenesheli, et al. Geometry-informed neural operator for large-scale 3d pdes. *Advances in Neural Information Processing Systems*, 36, 2024.

[57] B. List, L.-W. Chen, K. Bali, and N. Thuerey. How temporal unrolling supports neural physics simulators. *arXiv preprint arXiv:2402.12971*, 2024.

[58] B. Liu, N. Kovachki, Z. Li, K. Azizzadenesheli, A. Anandkumar, A. M. Stuart, and K. Bhat-tacharya. A learning-based multiscale method and its application to inelastic impact problems. *Journal of the Mechanics and Physics of Solids*, 158:104668, 2022.

[59] S. Liu, Y. Li, Z. Li, Z. Zheng, C. Duan, Z.-M. Ma, O. Yaghi, A. Anandkumar, C. Borgs, J. Chayes, et al. Symmetry-informed geometric representation for molecules, proteins, and crystalline materials. *Advances in Neural Information Processing Systems*, 36, 2024.

[60] Y. Liu, A. Sholokhov, H. Mansour, and S. Nabi. Physics-informed koopman network for time-series prediction of dynamical systems. In *ICLR 2024 Workshop on AI4DifferentialEquations In Science*, 2024.

[61] M. Liu-Schiaffini, J. Berner, B. Bonev, T. Kurth, K. Azizzadenesheli, and A. Anandkumar. Neural operators with localized integral and differential kernels. *arXiv preprint arXiv:2402.16845*, 2024.

[62] L. Lu, P. Jin, G. Pang, Z. Zhang, and G. E. Karniadakis. Learning nonlinear operators via deeponet based on the universal approximation theorem of operators. *Nature machine intelligence*, 3(3):218–229, 2021.

[63] D. J. Lucia, P. S. Beran, and W. A. Silva. Reduced-order modeling: new approaches for computational physics. *Progress in aerospace sciences*, 40(1-2):51–117, 2004.

[64] P. Ma, P. Y. Chen, B. Deng, J. B. Tenenbaum, T. Du, C. Gan, and W. Matusik. Learning neural constitutive laws from motion observations for generalizable pde dynamics. In *International Conference on Machine Learning*, pages 23279–23300. PMLR, 2023.

[65] Q. Ma, H. Wu, L. Xing, J. Wang, and M. Long. Eulagnet: Eulerian fluid prediction with lagrangian dynamics. *arXiv preprint arXiv:2402.02425*, 2024.

[66] H. A. Majid and F. Tudisco. Mixture of neural operators: Incorporating historical information for longer rollouts. In *ICLR 2024 Workshop on AI4DifferentialEquations In Science*, 2024.

[67] Z. Mao, A. D. Jagtap, and G. E. Karniadakis. Physics-informed neural networks for high-speed flows. *Computer Methods in Applied Mechanics and Engineering*, 360:112789, 2020.

[68] R. Maulik, B. Lusch, and P. Balaprakash. Reduced-order modeling of advection-dominated systems with recurrent neural networks and convolutional autoencoders. *Physics of Fluids*, 33(3):037106, 03 2021.

[69] J. J. Monaghan. Smoothed particle hydrodynamics. In: *Annual review of astronomy and astrophysics*. Vol. 30 (A93-25826 09-90), p. 543-574., 30:543–574, 1992.

[70] S. Munteanu, J. Rajadas, C. Nam, and A. Chattopadhyay. A volterra kernel reduced-order model approach for nonlinear aeroelastic analysis. In *46th AIAA/ASME/ASCE/AHS/ASC Structures, Structural Dynamics and Materials Conference*, page 1854, 2005.

[71] H. C. Nam, J. Berner, and A. Anandkumar. Solving Poisson equations using neural walk-on-spheres. *arXiv preprint arXiv:2406.03494*, 2024.

[72] R. Ni and A. H. Qureshi. Ntfields: Neural time fields for physics-informed robot motion planning. *arXiv preprint arXiv:2210.00120*, 2022.

[73] S. Pan, S. L. Brunton, and J. N. Kutz. Neural implicit flow: a mesh-agnostic dimensionality reduction paradigm of spatio-temporal data. *Journal of Machine Learning Research*, 24(41):1–60, 2023.

[74] J. Pathak, S. Subramanian, P. Harrington, S. Raja, A. Chattopadhyay, M. Mardani, T. Kurth, D. Hall, Z. Li, K. Azizzadenesheli, et al. Fourcastnet: A global data-driven high-resolution weather model using adaptive fourier neural operators. *arXiv preprint arXiv:2202.11214*, 2022.

[75] B. Peherstorfer. Breaking the kolmogorov barrier with nonlinear model reduction. *Notices of the American Mathematical Society*, 69(5):725–733, 2022.

[76] B. Peherstorfer and K. Willcox. Dynamic data-driven reduced-order models. *Computer Methods in Applied Mechanics and Engineering*, 291:21–41, 2015.

[77] J. Peng, H. Viswanath, K. Tiwari, and A. Bera. Graph-based decentralized task allocation for multi-robot target localization. *arXiv preprint arXiv:2309.08896*, 2023.

[78] A. Peyvan, V. Oommen, A. D. Jagtap, and G. E. Karniadakis. Riemannonets: Interpretable neural operators for riemann problems. *arXiv preprint arXiv:2401.08886*, 2024.

[79] T. Pfaff, M. Fortunato, A. Sanchez-Gonzalez, and P. W. Battaglia. Learning mesh-based simulation with graph networks. *arXiv preprint arXiv:2010.03409*, 2020.

[80] F. Pichi, B. Moya, and J. S. Hesthaven. A graph convolutional autoencoder approach to model order reduction for parametrized pdes. *Journal of Computational Physics*, 501:112762, 2024.

[81] M. A. Rahman, M. A. Florez, A. Anandkumar, Z. E. Ross, and K. Azizzadenesheli. Generative adversarial neural operators. *arXiv preprint arXiv:2205.03017*, 2022.

[82] M. A. Rahman, R. J. George, M. Elleithy, D. Leibovici, Z. Li, B. Bonev, C. White, J. Berner, R. A. Yeh, J. Kossaifi, et al. Pretraining codomain attention neural operators for solving multiphysics pdes. *arXiv preprint arXiv:2403.12553*, 2024.

[83] M. A. Rahman, J. Ghosh, H. Viswanath, K. Azizzadenesheli, and A. Bera. Pacmo: Partner dependent human motion generation in dyadic human activity using neural operators. *arXiv preprint arXiv:2211.16210*, 2022.

[84] M. A. Rahman and R. A. Yeh. Truly scale-equivariant deep nets with fourier layers. *Advances in Neural Information Processing Systems*, 36, 2024.

[85] M. Raissi, P. Perdikaris, and G. E. Karniadakis. Physics-informed neural networks: A deep learning framework for solving forward and inverse problems involving nonlinear partial differential equations. *Journal of Computational Physics*, 378:686–707, 2019.

[86] D. E. Raveh. Reduced-order models for nonlinear unsteady aerodynamics. *AIAA journal*, 39(8):1417–1429, 2001.

[87] L. Richter and J. Berner. Robust sde-based variational formulations for solving linear pdes via deep learning. In *International Conference on Machine Learning*, pages 18649–18666. PMLR, 2022.

[88] M. Salvador, L. Dede, and A. Manzoni. Non intrusive reduced order modeling of parametrized pdes by kernel pod and neural networks. *Computers & Mathematics with Applications*, 104:1–13, 2021.

[89] A. Sanchez-Gonzalez, J. Godwin, T. Pfaff, R. Ying, J. Leskovec, and P. Battaglia. Learning to simulate complex physics with graph networks. In *International conference on machine learning*, pages 8459–8468. PMLR, 2020.

[90] R. Sarkar, K. S. S. Aripirala, V. S. Jadhav, S. S. Sakhinana, and V. Runkana. Pointsage: Mesh-independent superresolution approach to fluid flow predictions. In *ICLR 2024 Workshop on AI4DifferentialEquations In Science*, 2024.

[91] B. Schölkopf and A. J. Smola. *Learning with kernels: support vector machines, regularization, optimization, and beyond*. MIT press, 2002.

[92] B. Shih, A. Peyvan, Z. Zhang, and G. E. Karniadakis. Transformers as neural operators for solutions of differential equations with finite regularity, 2024.

[93] K. Shukla, V. Oommen, A. Peyvan, M. Penwarden, N. Plewacki, L. Bravo, A. Ghoshal, R. M. Kirby, and G. E. Karniadakis. Deep neural operators as accurate surrogates for shape optimization. *Engineering Applications of Artificial Intelligence*, 129:107615, 2024.

[94] J. Sirignano and K. Spiliopoulos. DGM: A deep learning algorithm for solving partial differential equations. *Journal of computational physics*, 375:1339–1364, 2018.

[95] B. Smith, F. D. Goes, and T. Kim. Stable neo-hookean flesh simulation. *ACM Transactions on Graphics (TOG)*, 37(2):1–15, 2018.

[96] M. Stoffel, F. Bamer, and B. Markert. Deep convolutional neural networks in structural dynamics under consideration of viscoplastic material behaviour. *Mechanics Research Communications*, 108:103565, 2020.

[97] B. Ummenhofer, L. Prantl, N. Thuerey, and V. Koltun. Lagrangian fluid simulation with continuous convolutions. In *International Conference on Learning Representations*, 2020.

[98] R. Vinuesa and S. L. Brunton. The potential of machine learning to enhance computational fluid dynamics. *arXiv preprint arXiv:2110.02085*, pages 1–13, 2021.

[99] H. Viswanath, M. A. Rahman, R. Bhaskara, and A. Bera. Adafnio: Adaptive fourier neural interpolation operator for video frame interpolation. *arXiv preprint arXiv:2211.10791*, 2022.

- [100] H. Viswanath, M. A. Rahman, A. Vyas, A. Shor, B. Medeiros, S. Hernandez, S. E. Prameela, and A. Bera. Neural operator: Is data all you need to model the world? an insight into the impact of physics informed machine learning. *arXiv preprint arXiv:2301.13331*, 2023.
- [101] S. Wang, J. H. Seidman, S. Sankaran, H. Wang, G. J. Pappas, and P. Perdikaris. Bridging operator learning and conditioned neural fields: A unifying perspective. *arXiv preprint arXiv:2405.13998*, 2024.
- [102] T. Wen, K. Lee, and Y. Choi. Reduced-order modeling for parameterized pdes via implicit neural representations. *arXiv preprint arXiv:2311.16410*, 2023.
- [103] C. White, J. Berner, J. Kossaifi, M. Elleithy, D. Pitt, D. Leibovici, Z. Li, K. Azizzadenesheli, and A. Anandkumar. Physics-informed neural operators with exact differentiation on arbitrary geometries. In *The Symbiosis of Deep Learning and Differential Equations III*, 2023.
- [104] A. Wikner, J. Harvey, M. Girvan, B. R. Hunt, A. Pomerance, T. Antonsen, and E. Ott. Stabilizing machine learning prediction of dynamics: Novel noise-inspired regularization tested with reservoir computing. *Neural Networks*, 170:94–110, 2024.
- [105] H. Wu, F. Xu, Y. Duan, Z. Niu, W. Wang, G. Lu, K. Wang, Y. Liang, and Y. Wang. Spatio-temporal fluid dynamics modeling via physical-awareness and parameter diffusion guidance. *arXiv preprint arXiv:2403.13850*, 2024.
- [106] Y. Xie, T. Takikawa, S. Saito, O. Litany, S. Yan, N. Khan, F. Tombari, J. Tompkin, V. Sitzmann, and S. Sridhar. Neural fields in visual computing and beyond. In *Computer Graphics Forum*, volume 41, pages 641–676. Wiley Online Library, 2022.
- [107] M. Xu, J. Han, A. Lou, J. Kossaifi, A. Ramanathan, K. Azizzadenesheli, J. Leskovec, S. Ermon, and A. Anandkumar. Equivariant graph neural operator for modeling 3d dynamics. *arXiv preprint arXiv:2401.11037*, 2024.
- [108] Y. Yin, M. Kirchmeyer, J.-Y. Franceschi, A. Rakotomamonjy, and patrick gallinari. Continuous PDE dynamics forecasting with implicit neural representations. In *The Eleventh International Conference on Learning Representations*, 2023.
- [109] M. Zefran and F. Bullo. Lagrangian dynamics. *Robotics and Automation Handbook*, pages 5–1, 2005.
- [110] Q. Zhou and A. Jacobson. Thingi10k: A dataset of 10,000 3d-printing models, 2016.

A Additional related works

Time series dynamical systems Simulating temporal dynamics in an auto-regressive manner is a particularly challenging task due to error accumulations during long rollout [57, 104]. There have been many works that learn temporal PDEs and CFD, including [39, 40, 42, 60, 65, 66, 90, 105]. Some works have proposed neural network-based approaches to model 3D Lagrangian dynamics, such as [97], who propose a convolutional neural network-based approach to model the behavior of Newtonian fluids in 3D systems. [89] propose a more general graph-based framework, but the network suffers from high computation time on very dense graphs.

B Background

B.1 Operator learning

Here, we summarize the important ingredients of neural operators. For more details, please refer to [53]. Operator learning is a machine learning paradigm where a neural network is trained to map between infinite-dimensional function spaces. Let $\mathcal{G} : \mathcal{V} \rightarrow \mathcal{A}$ be a nonlinear map between the two function spaces \mathcal{V} and \mathcal{A} . A neural operator is an operator parameterized by a neural network given by $\mathcal{G}_\theta : \mathcal{V} \rightarrow \mathcal{A}$, $\theta \in \mathbb{R}^z$, that approximates this function mapping in the finite-dimensional space. The learning problem can be formulated as $\min_{\theta \in \mathbb{R}^z} \mathbb{E}_{v \sim D} [\|\mathcal{G}_\theta(v) - \mathcal{G}(v)\|_{\mathcal{V}}^2]$, where $\|\cdot\|_{\mathcal{V}}$ is a norm on \mathcal{V} and D is a probability distribution on \mathcal{V} . In practice, the above optimization is posed as an empirical risk-minimization problem, defined as $\min_{\theta \in \mathbb{R}^P} \frac{1}{N} \sum_{i=1}^N \|\mathcal{G}_\theta(v^{(i)}) - a^{(i)}\|_{\mathcal{V}}^2$.

B.2 Kernel methods and manifold learning

Kernel methods have been applied in manifold learning, where they serve as tools for constructing operators that act on functions defined over sampled data. Many such methods—including diffusion maps and Laplacian eigenmaps—can be interpreted as variants of kernel PCA [38].

Belkin and Niyogi [7] and Coifman et al. [20] studied *radially symmetric* kernels of the form $k(x, y) = h\left(\frac{\|x-y\|^2}{\varepsilon}\right)$ where $h : \mathbb{R}_+ \rightarrow \mathbb{R}$ is a decreasing function, typically Gaussian. These kernels are *local*. As such, they are isotropic and spatially invariant [10].

Neural operator literature defines the kernel based **kernel integral transform**:

$$(\mathcal{K}f)(x) = \int_{\Omega} k(x, y) f(y) dy,$$

which is central to both manifold learning and neural operator frameworks. It maps input functions $f : \Omega \rightarrow \mathbb{R}^d$ to output functions via integration against k , and serves as the foundation for approximating function-to-function mappings.

In the context of manifold learning, local radially symmetric kernels induce a geometry on the embedded manifold. As the sample density increases, the kernel implicitly defines a metric structure through its interactions over neighborhoods on the manifold [10]. Consequently, such kernels not only enable dimensionality reduction but also act as geometric priors over data manifolds.

Finally, this kernel framework extends naturally to operator learning, where local solution maps—such as those arising from hyperbolic PDEs—can be effectively approximated using locally supported kernels [61].

B.3 Kernel preliminaries

Let $\Omega \subset \mathbb{R}^n$ and let $f : \Omega \rightarrow \mathbb{R}^d$ be a continuous function. We assume $f \in \mathcal{H}_K$, where \mathcal{H}_K is a Reproducing Kernel Hilbert Space (RKHS) over Ω , associated with a kernel $K : \Omega \times \Omega \rightarrow \mathbb{R}$. For all $x \in \Omega$, the evaluation functional $L_x : f \mapsto f(x)$ is bounded and there exists a unique sample $K(x, \cdot) \in \mathcal{H}_K$ satisfying the reproducing property:

$$f(x) = \langle f, K(x, \cdot) \rangle_{\mathcal{H}_K}, \quad \forall f \in \mathcal{H}_K.$$

In particular, the kernel satisfies

$$\langle K(x, \cdot), K(y, \cdot) \rangle_{\mathcal{H}_K} = K(x, y), \quad \forall x, y \in \Omega,$$

which follows directly from the reproducing property.

Let $X = \{x_1, \dots, x_r\} \subset \Omega$ be a set of sample locations, and define the vector space of functions

$$\mathcal{H}_X := \text{span}\{K(x_i, \cdot) \mid x_i \in X\} = \left\{ \sum_{i=1}^N c_i K(x_i, \cdot) \mid x_i \in \Omega, c_i \in \mathbb{R}, N \in \mathbb{N} \right\} \subset \mathcal{H}_K.$$

The reproduction property implies that any $f \in \mathcal{H}_X$ allows for pointwise evaluation, given by the form

$$\langle f, K_x \rangle = f(x)$$

$$f(x) = \sum_{i=1}^r c_i K(x_i, x), \quad c_i \in \mathbb{R}.$$

The RKHS action is presented in the integral transform operator \mathcal{K} [54] defined by

$$(\mathcal{K}f)(x) := \int_{\Omega} K(x, y) f(y) dy,$$

which we discretize. For a neighborhood $\mathcal{N}(x) \subset X$, we write

$$f(x) \approx \sum_{x_j \in \mathcal{N}(x)} w_j(x) K(x, x_j) f(x_j).$$

Replacing the kernel-weight product with a learned approximation, we introduce a parametric kernel $\psi_\theta : \Omega \times \Omega \rightarrow \mathbb{R}$, yielding the estimator

$$\hat{f}(x) := \sum_{x_j \in \mathcal{N}(x)} \psi_\theta(x, x_j) f(x_j).$$

This form approximates $\langle f, K(x, \cdot) \rangle_{\mathcal{H}_K}$ using a localized, data-driven surrogate ψ_θ in place of analytic kernels. Training proceeds by minimizing the empirical reconstruction loss over a set of query points:

$$\mathcal{L}_{\text{recon}} = \sum_{x \in \Omega_{\text{train}}} \left\| \hat{f}(x) - f(x) \right\|^2,$$

where \hat{f} is computed via the learned kernel estimator above. When $\psi_\theta(x, x_j) \rightarrow K(x, x_j)$ and $\mathcal{N}(x) = X$, the estimator recovers the exact RKHS interpolant.

This construction provides a localized, continuous, and mesh-free approximation of the RKHS projection operator. The reproducing property guarantees the estimator recovers pointwise field values. For more background on RKHS and kernel approximation, see [9, 91].

B.4 Graph interaction network

The graph interaction network proposed in [5] learns a relation-centric function f that encodes spatial interactions between the interacting nodes within a system as a function of their interaction attributes r . This can be represented as $e_{t+1} = f_R(x_{1,t}, x_{2,t}, r)$. A node-centered function predicts the temporal dynamics of the node as a function of the spatial interactions as follows $x_{1,t+1} = f_o(e_{t+1}, x_{1,t})$. In a system of m nodes, the spatial interactions are represented as a graph, where the neighborhood is defined by a ball of radius r . This graph is represented as $G(O, R)$, where O is the collection of objects and R is the relationships between them. The interaction between them is defined as $\mathcal{I}(G) = f_o(a(G, X, f_R(\langle x_i, x_j, r_{ij} \rangle)))$, Where a is an aggregation function that combines all the interactions, X is the set of external effects, not part of the system, such as gravitational acceleration, etc.

C Algorithms

The following section presents key algorithms that are helpful for implementing the concepts presented in the paper

Algorithm 1 Kernel Integral Transform [56], Neural Operator Library

Input:

- $x \in \mathbb{R}^{m \times d}$ // Query points
- $y \in \mathbb{R}^{n \times d}$ // Support points
- $f_y \in \mathbb{R}^{n \times r}$ (optional) // Function values
- **neighbors** // CSR format: indices and row splits
- $k(\cdot)$ // Parametrized kernel (e.g., MLP)
- $\text{type} \in \{\text{linear, nonlinear, ...}\}$ // Transform type
- $\text{weights} \in \mathbb{R}^n$ (optional)

Output:

- $\text{out} \in \mathbb{R}^{m \times r}$ // Transformed values

- 1: **if** x is None **then**
- 2: $x \leftarrow y$
- 3: **end if**
- 4: $y_{\text{nb}} \leftarrow y[\text{neighbors.indices}]$
- 5: **if** f_y is given **then**
- 6: $f_{\text{nb}} \leftarrow f_y[\text{neighbors.indices}]$
- 7: **end if**
- 8: $\text{num_reps} \leftarrow \text{neighbors.row_splits}[1:] - \text{neighbors.row_splits}[:-1]$
- 9: $x_{\text{rep}} \leftarrow \text{repeat_interleave}(x, \text{num_reps})$
- 10: $\phi \leftarrow \text{concat}(x_{\text{rep}}, y_{\text{nb}})$
- 11: **if** type is nonlinear and f_y is given **then**
- 12: $\phi \leftarrow \text{concat}(\phi, f_{\text{nb}})$
- 13: **end if**
- 14: $\kappa \leftarrow k(\phi)$ ▷ Apply kernel function
- 15: **if** f_y is given and type \neq nonlinear_kernelonly **then**
- 16: $\kappa \leftarrow \kappa \cdot f_{\text{nb}}$
- 17: **end if**
- 18: **if** weights are given **then**
- 19: $\kappa \leftarrow \text{weights}[\text{neighbors.indices}] \cdot \kappa$
- 20: reduction \leftarrow sum
- 21: **else**
- 22: reduction \leftarrow mean
- 23: **end if**
- 24: $\text{out} \leftarrow \text{segment_csr}(\kappa, \text{neighbors.row_splits}, \text{reduction})$
- 25: **return** out

Algorithm 2 Kernel-based ROM Inference

Input:

- $\text{sampled_ic} \in \mathbb{R}^{m \times d}$ // Sampled initial points
- $\text{full_ic} \in \mathbb{R}^{n \times d}$ // Full initial state
- $\text{sampled_f} \in \mathbb{R}^{m \times d}$ // Initial state in sampled space
- radius // Neighborhood radius

Output:

- $\text{out} \in \mathbb{R}^{n \times d}$ // Updated ROM state

- 1: $\text{neighbors} \leftarrow \text{NeighborSearch}(\text{sampled_ic}, \text{full_ic}, \text{radius})$
- 2: $\text{out} \leftarrow \text{IntegralTransform.forward}(x = \text{full_ic}, y = \text{sampled_ic}, f_y = \text{sampled_f}, \text{neighbors})$
- 3: **return** out

Algorithm 3 GNN Time-Stepper Inference

Input:

$G = (V, E)$: input graph with nodes V and edges E
 $x \in \mathbb{N}^{|V| \times 1}$: categorical node types
 $p \in \mathbb{R}^{|V| \times d}$: recent positions and velocities
 $e \in \mathbb{R}^{|E| \times d_e}$: edge attributes (displacement, distance)
 $\text{edge_index} \in \mathbb{N}^{2 \times |E|}$: sender and receiver indices
 $\text{recent_pos} \in \mathbb{R}^{|V| \times d}$: current position of each node

Output:

$\hat{a} \in \mathbb{R}^{|V| \times r}$: predicted acceleration (or equivalent output)

```
1: Step 1: Node and Edge Feature Initialization
2:  $h_v \leftarrow \text{concat}(\text{EmbedType}(x), p)$   $\triangleright$  Embed categorical type and concatenate with pos/velocity
3:  $h_v \leftarrow \text{NodeInputMLP}(h_v)$ 
4:  $h_e \leftarrow \text{EdgeInputMLP}(e)$ 
5: Step 2: Message Passing (Encoder)
6: for  $i = 1$  to  $n_{\text{mp\_layers}}$  do
7:    $h_v, h_e \leftarrow \text{GNNLayer}_i(h_v, \text{edge\_index}, h_e, \text{node\_dist})$ 
8: end for
9: Step 3: Global Transformation via GNOT Layer
10:  $h_v \leftarrow \text{GNOTLayer}(h_v, \text{recent\_pos})$ 
11: Step 4: Message Passing (Decoder)
12: for  $i = 1$  to  $n_{\text{mp\_layers}}$  do
13:    $h_v, h_e \leftarrow \text{GNNLayerOut}_i(h_v, \text{edge\_index}, h_e, \text{node\_dist})$ 
14: end for
15: Step 5: Node-wise Output Projection
16:  $\hat{a} \leftarrow \text{NodeOutputMLP}(h_v)$ 
17: return  $\hat{a}$ 
```

D Architecture outline

The schematic in fig. 6 illustrates the full sequence of operations performed during a single time-step of the proposed method. It delineates the interaction between the time-stepping mechanism, the kernel-based reduced-order model (kernel-ROM), the Euler integration scheme, and the spatial sampling strategy used to update the system state.

E Experimental setup details

E.1 ϕ_Θ setup and Hyperparameters

Data representation To train ϕ_Θ , we create a window of w point cloud velocity sequences as the input defined on the nodes, with the pointwise acceleration as the output. We define $\{\mathbf{x}_t^i\} \in \mathbb{R}^{r \cdot d}$ to be the pointwise positions of r particles within a d -dimensional system at time t . A sequence of T time steps is denoted as $\mathbf{x}_{0:T} = (\mathbf{x}_0, \dots, \mathbf{x}_T)$. In particular, $\{\mathbf{x}_t^0, \dots, \mathbf{x}_t^r\}$ are the individual particles within the system at time t . We define velocity at time n as \mathbf{v}_t as $\mathbf{x}_t - \mathbf{x}_{t-1}$. Similarly, acceleration at time n is defined as $\mathbf{a}_t = \mathbf{v}_t - \mathbf{v}_{t-1}$. In all these cases, Δt is set to one for simplicity. To train the model, we follow the same procedure as [89]. We additionally encode the particle types (water, sand, plasticine, etc.) as embeddings, which is useful for multimaterial simulations. The graph is constructed as a `radius_graph`, defined within `pytorch_geometric` library.

Boundary representation To enforce the boundaries of the system, the node feature includes the past w velocity fields as well as the distance of the most recent position field to the upper (b_u) and lower (b_l) boundaries of the computational domain, given by $\mathcal{D} = [(x - b_l)/\rho, (b_u - x)/\rho], \forall x$, where ρ is the radius of the graph.

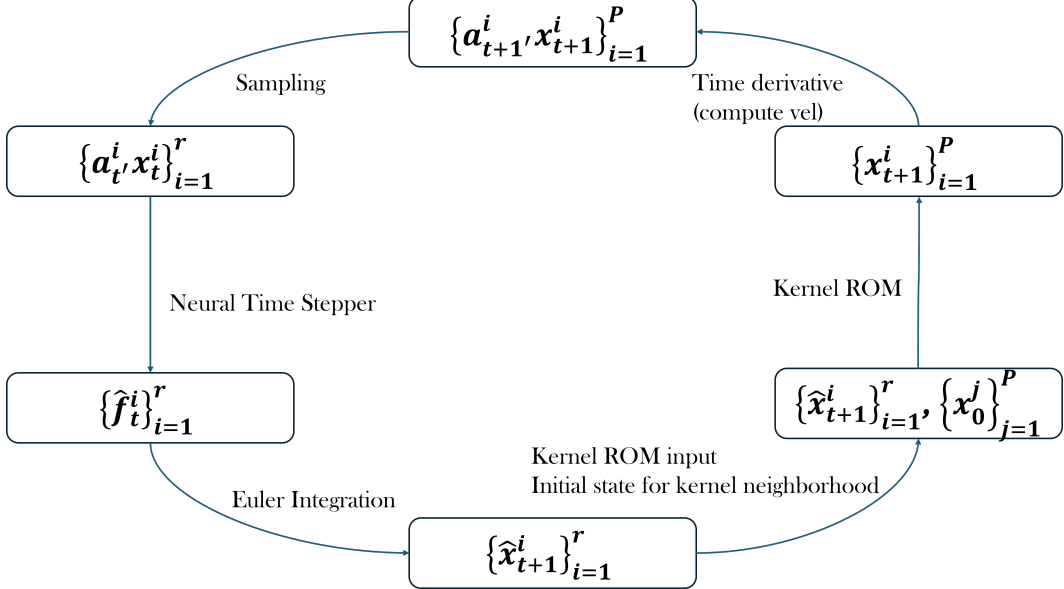


Figure 6: **Single-step flow diagram:** Overview of the forward pass used to infer the system state at the next time-step via Kernel-ROM, time-stepping, Euler integration, and spatial sampling. As ϕ_Θ takes as input a window of past-states, we require the same set of samples for a trajectory evolution

E.2 Hyperparameters

The models were implemented using Pytorch library and trained on CUDA. The graphs were built using Pytorch Geometric module. All models were trained on NVIDIA RTX 3060 GPUs.

ϕ_Θ time-stepper The graph is constructed using `radius_graph` defined in Pytorch Geometric. The node features and the edge features, which include the distance from the boundary points, are encoded into latent vectors of size 128 using 2 MLPs. The encoder uses two layers of interaction network. The latents are then processed by two layers of Neural Operator Transformer. The decoder layers are symmetric to the encoder layers. The NOT block uses 4 attention heads, branch and trunk sizes of 32, and an output dim of 128.

Kernel-ROM The network uses discrete integral transform, available within the neural operator library. The model uses linear kernel transformations with `gelu` activations. The model uses a sequence of MLP layers to parameterize the kernel, with varying channels for each physical system. It is set to [32, 64] (most systems), [128, 256] (fluid). The neighborhood radius is a tuned hyperparameter, that varies with sample size.

Optimizers Optimization is done with Adamax optimizer, with an initial learning rate of 1e-4, weight decay of 1e-6 and a batch size of 4. The learning rate was decayed exponentially from 10^{-4} to 10^{-6} using a scheduler, with a gamma of $0.1^{1/5e6}$

F Additional dataset details

We model the following classes of materials - elastic, plasticine, granular, Newtonian fluids, non-Newtonian fluids, and multi-material simulations. Notably, this framework is compatible with data generated using different solvers such as Finite Element Method (FEM) [37], Material Point Method (MPM) [41], or Smooth Particle Hydrodynamics (SPH) [69].

Plasticine (von Mises Yield) Using the NCLAW simulator, we generated 100 trajectories of 400 time steps ($dt = 5e-4$) with random initial velocities and 4 different geometries - Stanford bunny, Stanford armadillo, blub (goldfish), and spot (cow). The trajectories are modeled using Saint Venant-Kirchoff

elastic model, given by

$$\mathbf{P} = \mathbb{U}(2\mu\epsilon + \lambda tr(\epsilon))\mathbb{U}^T \quad (9)$$

where λ and μ are Lamé constants, \mathbf{P} is the second Piola-Kirchoff stress and ϵ is the strain. \mathbb{U} is obtained by applying SVD to the deformation gradient $\mathbf{F} = \mathbb{U}\Sigma\mathbf{V}^T$. The von Mises yield condition is denoted by

$$\delta\gamma = \|\hat{\epsilon}\| - \frac{\tau_Y}{2\mu} \quad (10)$$

where ϵ is the normalized Henky strain, τ_Y is the yield stress.

Granular material (Drucker Prager sand flows) We trained the model on 2 datasets to simulate granular media. We generated 100 trajectories at 300 time steps, using NCLAW simulator and on the 2D Sand dataset released by [79]. The Drucker-Prager elastoplasticity is modeled by the same Saint Venant–Kirchhoff elastic model, given by Equation 9. Additionally, the Drucker-Prager yield condition is applied such that

$$tr(\epsilon) > 0 \quad \text{or} \quad \delta\gamma = \|\hat{\epsilon}\| + \alpha \frac{(3\lambda + 2\mu)tr(\epsilon)}{2\mu} > 0 \quad (11)$$

where, $\alpha = \sqrt{2/3} \frac{2\sin\theta}{3-\sin\theta}$ and θ is the frictional angle of the granular media.

Elasticity To simulate elasticity, we generated simulations using meshes from Thingi10k dataset [110]. We generated 24 trajectories, with 200 time steps, for 6 geometries to train the model. The elasticity is modeled using stable neo-Hookean model, as proposed in [95]. The energy is denoted by

$$\Psi = \frac{\mu}{2}(I_C - 3) + \frac{\lambda}{2}(J - \alpha)^2 - \frac{\mu}{2}\log(I_C + 1) \quad (12)$$

where I_C refers to the first right Cauchy-Green invariant and J is the relative volume change. μ and λ are Lamé constants. The corresponding Piola-Kirchoff stress is given by

$$\mathbf{P} = \mu\left(1 - \frac{1}{I_C + 1}\right)\mathbf{F} + \lambda(J - \alpha)\frac{\partial J}{\partial \mathbf{F}} \quad (13)$$

where \mathbf{F} is the deformation gradient.

Newtonian fluids For Newtonian fluids, In the 2D setting, we use WaterDrop dataset created by [79], which is generated using the material point method (MPM). For the 3D setting, we generated 100 trajectories with random initial velocity, each spanning 1000 time steps at a dt of $5e-3$. This dataset was prepared using the NCLAW framework. These are modeled as weakly compressible fluids, using fixed corotated elastic model with $\mu = 0$. The Piola-Kirchoff Stress is given by

$$\mathbf{P} = \lambda J(J - 1)\mathbf{F}^{-T} \quad (14)$$

Non-Newtonian fluids To train the model on non-Newtonian fluids, we used the Goop and Goop-3D datasets.

Multimaterial We simulated multi-material trajectories in 2D using the dataset published by [79].

G Training setup

Time-stepper We follow the exact training procedure outlined in [89] for ϕ_Θ . We use the 1-step loss function over a pair of consecutive time steps k and $k + 1$, imposing a strong inductive bias towards a Markovian system. Each system is trained for 5 million steps.

The model is validated by full rollouts on 10 held-out validation sets per material simulation, with performance measured by the MSE between predicted particle positions and ground-truth particle positions.

Kernel-ROM To train the Kernel-ROM, we define the neighborhood over samples defined at $t = 0$, i.e. $\{x_0^i\}_{i=1}^P$ and $\{x_0^j\}_{j=1}^r$. For all the subsequent time-steps, we leverage this neighborhood. This enables us to evolve $\{\hat{f}\}$ using the spatial information of the state at $t = 0$. The input function for the model is point-wise positions at a given time-step t for non-fluid systems and deformation $x_t - x_0$ for fluid systems. We generate these using ϕ_Θ . Each system is trained for 30,000 steps and evaluated on unseen discretizations and trajectories.

H Additional results

2D simulations Figure 7 presents qualitative comparisons between ground truth and $(P \cdot d)$ -point predictions produced by GIOROM on various 2D simulations. The subfigures depict a range of dynamic behaviors: (a) granular flow, (b) soft body motion under gravity, (c) external force acting on a highly elastic material, and (d) coupled interactions between granular media and Newtonian fluids.

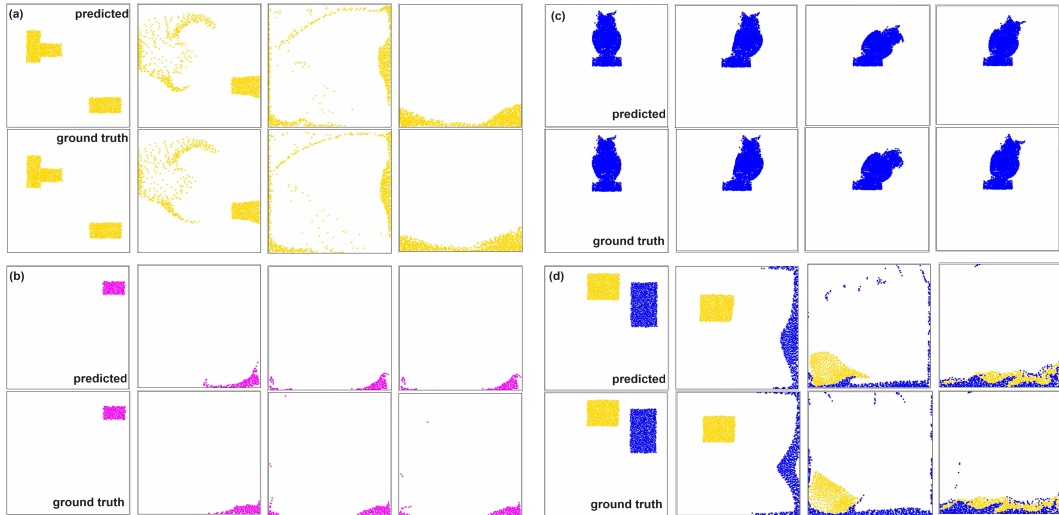


Figure 7: **2D point-cloud simulations:** $(P \cdot d)$ -point inference results using GIOROM. **(a)** Granular flow; **(b)** Soft body under gravity; **(c)** Elastic response to external force; **(d)** Coupled fluid-granular interactions.

3D simulations Visualizations of 3D dynamics are shown in fig. 8, illustrating the output of GIOROM across multiple material models. Figure 9 provides side-by-side comparisons of predicted versus ground-truth simulations for water and sand. Figure 10 further contrasts predictions in the sampled subspace against reconstructions over the full discretized domain.

I Ablations

Neural operator baselines We contrast the performance of our approach against other discretization invariant neural physics solvers. Table 3 represents the rollout performance of different Neural Operator models on sampled inputs. The performance is measured as the average MSE accumulated over the entire duration. We compare against **GINO** [56], General Neural Operator Transformer **GNOT** [33] and Inducing Point Operator Transformer [51]. Additionally, we compare against graph neural network based model **GNS** [89]. We show that our modified GNS performs similarly to the GNS. Interaction network based models are observed to outperform purely neural operator models, especially in highly dynamic simulations, due to better expressivity of interaction networks in capturing local information.

Speedup against graph neural networks Graph neural networks can effectively capture spatial interactions in point clouds. However, the message passing operation adds a computational overhead that we improve this with NOT layers. We show, in Table 4 and Table 5, that our model has faster inference times compared to GNNs.

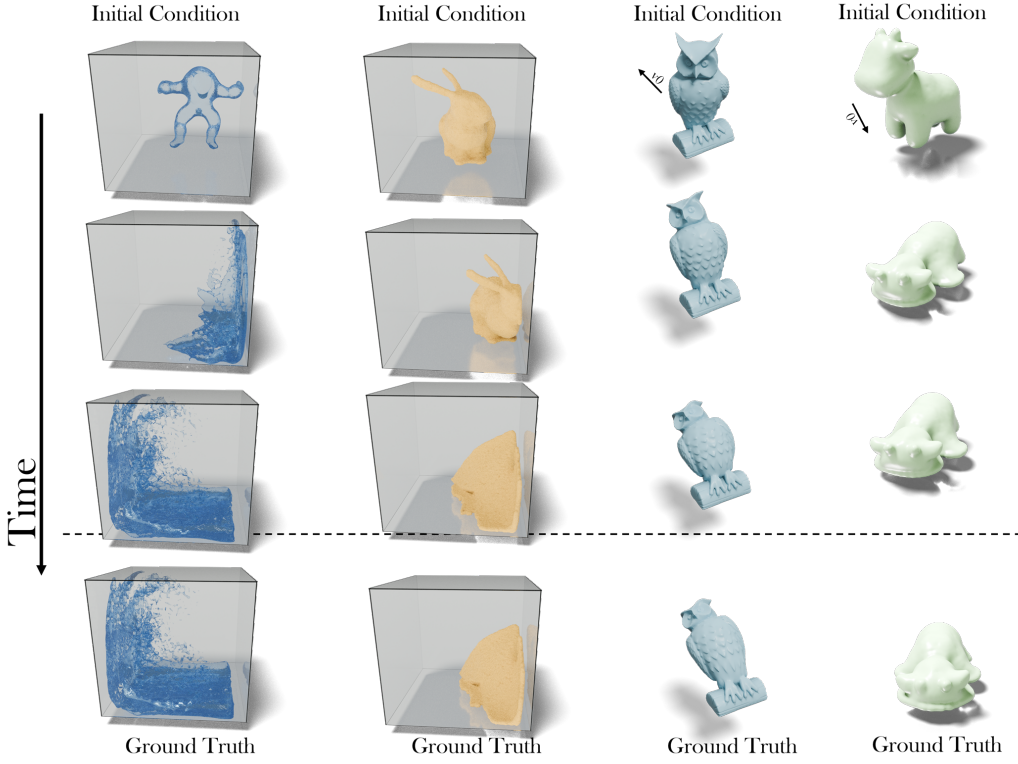


Figure 8: **3D physical simulations:** Time-evolved predictions for Newtonian fluid (water), Drucker-Prager (sand), von Mises (plasticine), and elastoplastic material models.

Table 3: This table compares the rollout MSE of ϕ_Θ against other neural physics solvers in the sampled space $\mathbb{R}^{r.d.}$.

MODEL	WATER-3D	PLASTICINE	ELASTIC	SAND-3D
GNS	0.0108	0.0038	0.0003	0.0008
GINO	0.38	0.09	0.18	0.07
GNOT	0.046	0.0052	0.0028	0.0085
IPOT	0.15	0.097	0.084	0.0075
ϕ_Θ	0.0106	0.0008	0.0004	0.0009

Table 4: Contrasting the change in computation time with the increase in connectivity radius for a graph with 7056 points. The times shown represent the overall time needed to infer all 200 time steps. We compare our time-stepper with other neural network based physics solvers.

MODEL	TIME STEPS	NUMBER OF SPATIAL POINTS	CONNECTIVITY RADIUS						
			0.040	0.050	0.060	0.070	0.080	0.090	0.100
OURS	200	7056 points	20.1s	34.3s	47.6s	65.8s	89.7s	104.1s	109.3s
GNS	200	7056 points	43.5s	73.5s	111.6s	162s	226.2s	305.9s	386.0s

Table 5: Contrasting the change in computation time with an increase in graph size at a fixed radius of 0.060. The times shown represent the overall time needed to infer 200 time steps. We compare our time-stepper against other neural network based physics solvers

MODEL	PARAMETERS	CONNECTIVITY	MATERIAL	TIME STEPS	GRAPH SIZE			
					1776 POINTS	4143 POINTS	5608 POINTS	7056 POINTS
OURS	4,312,247	0.060	Plasticine	200	3.9s	14.5s	27.3s	47.6s
GNS	1,592,987	0.060	Plasticine	200	7.8 s	38.3s	68.7s	111.6s

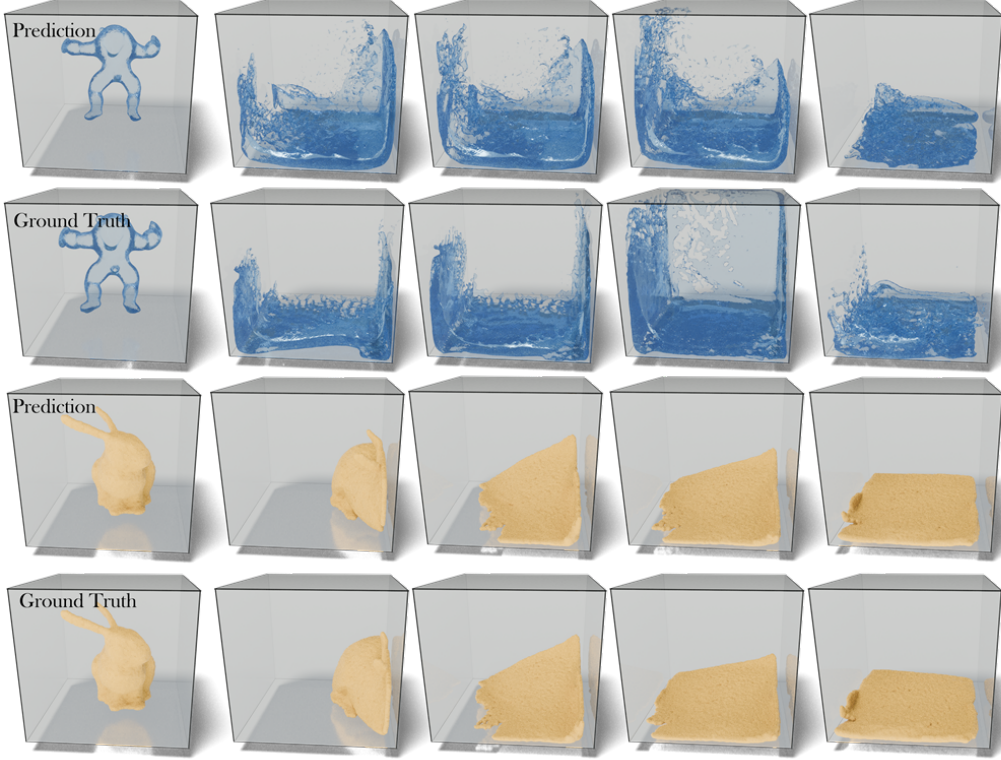


Figure 9: **Ground-truth comparisons:** Rendered outputs for water and sand simulations contrasted against reference solutions.

Table 6: Contrasting the inference times (in seconds) for highly dense point clouds up-sampled from highly sparse graphs (1776 points).

TIME STEPS	ROLLOUT SIZE	ROLLOUT TIME ϕ_Θ (s)	FULL-ORDER SIZE	UPSCALE TIME κ (s)
200	1776	3.9	7,000	5e-3
200	1776	3.9	40,000	3e-3
200	1776	3.9	60,000	8e-3
200	1776	3.9	100,000	9e-3

Number of message-passing layers We show that the key bottleneck in terms of speed is the message-passing operation within the Interaction Network encoder and decoder.

Table 7: This table shows that the number of message-passing layers results in a negligible improvement in rollout Loss.

NUM. MESSAGE PASSING LAYERS	CONNECTIVITY	INPUT SIZE	INFERENCE TIME/STEP	LOSS
2	0.077	2247	3.6	0.0008
4	0.077	2247	3.8	0.0009
6	0.077	2247	4.2	0.0014
8	0.077	2247	4.3	0.0009

I.1 Sampling strategy and rollout loss

We compared different sampling strategies against the rollout Loss (MSE). The results are presented in Table 8.

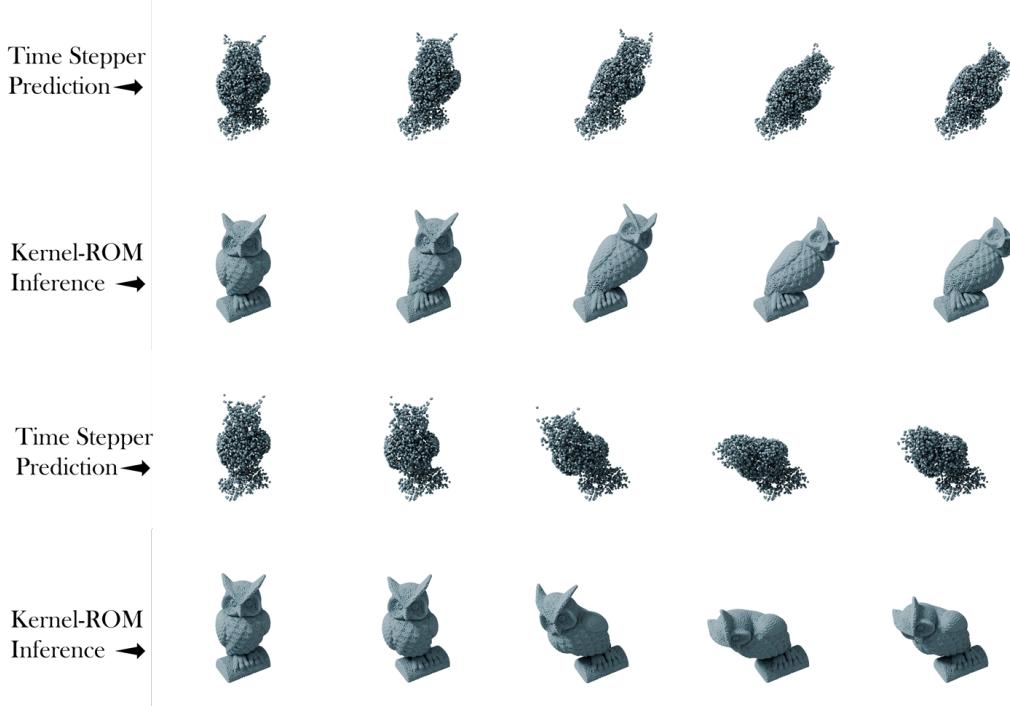


Figure 10: **Subspace vs full-space inference:** Rows 1 and 3 show predictions from the time-stepper on the sampled space; Rows 2 and 4 depict Kernel-ROM output projected back to the full discretization.

Table 8: Comparison of different sampling and graph construction strategies against rollout MSE on Water-2D dataset

SAMPLING STRATEGY	GRAPH TYPE	ROLLOUT MSE
RANDOM	RADIUS	0.0098
RANDOM	DELAUNAY	7.017
FPS	RADIUS	0.0097
FPS	DELAUNAY	8.04

J Additional discussions

J.1 Understanding the correlation between sparsification and performance

We study the relationship between performance and sample size to understand how the structural fidelity of the interaction graph degrades the predictions under extreme sparsifications. Our analysis focuses on a small Water2D system (678 particles), where the graph structure can be explicitly visualized using `networkx`, as well as a larger Plasticine3D system. We consider different sampling levels to examine how graph sparsification impacts this relationship.

Figure 11 presents rollout MSE at two sampling ratios—35% and 11%—for the Water2D system. At 35% sampling, we observe a trend: rollout MSE consistently drops with improving the connectivity. However, with further modifications to the radius, the MSE increases. This suggests that beyond a point, the addition of edges leads to degradations. The visual rollout in fig. 12 shows that improving connectivity improves the performance upto a limit.

In contrast, at 11% sampling, the rollout MSE remain high regardless of radius, and no clear trend emerges. As shown in fig. 13, the predicted rollouts diverge significantly from the ground truth. The third column in each frame represents the reduced-space ground truth at $(r \cdot d)$ points, which itself is visually and physically distinct from the full-resolution system. This indicates that at extreme

sparsity, the reduced graph fails to retain sufficient physical characteristics, rendering it unsuitable for accurate inference.

Figure 14 extends this analysis to the Plasticine3D system. At 22% sampling, we again observe that rollout MSE initially decreases, but as the radius increases further, this trend reverses. However, at 3.3% sampling, there is no correlation.

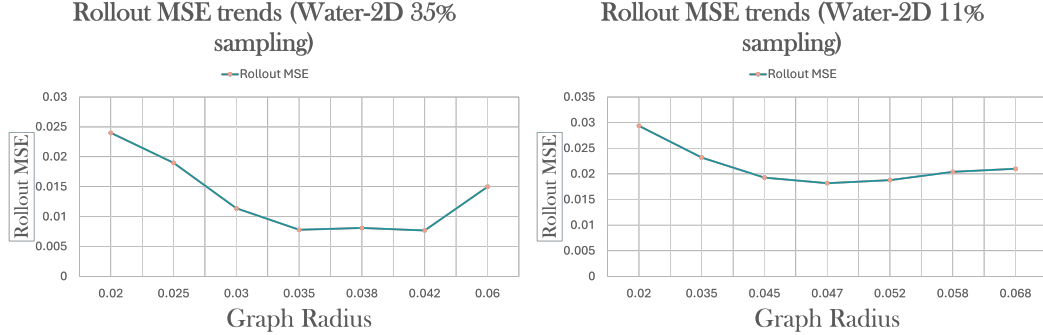


Figure 11: **Water2D: Radius vs. rollout MSE.** Left: 35% sampling. Right: At 11%, there is a weak correlation between them.

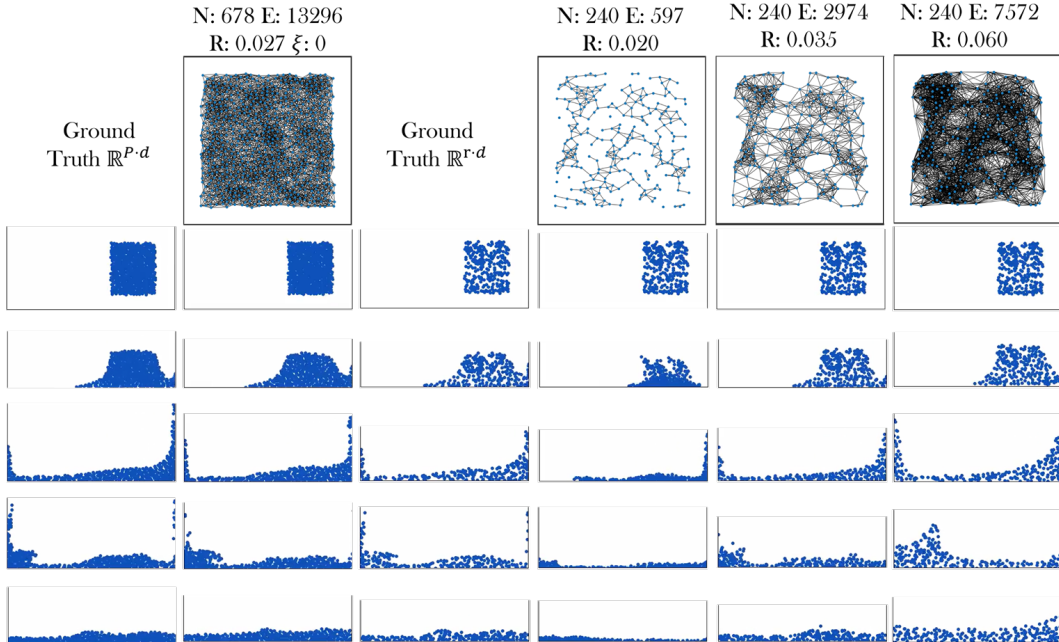


Figure 12: **Water2D at 35% sampling.** First two columns: full-space ground truth and prediction on $(P \cdot d)$ points. Third column: reduced-space ground truth at $(r \cdot d)$ points. Right columns: predictions at varying radii. Rollouts remain visually and physically consistent with the full system at $R=0.035$

J.2 Limitations of kernel-ROM to extreme sparsifications

The kernel-ROM model employs an implicit neural representation to approximate discrete kernel integral transforms over sparse point-wise function evaluations. However, under extreme sparsification, the quality of this representation degrades significantly.

When the number of supervised function evaluations is severely limited, increasing the neighborhood radius does not lead to meaningful improvements. Instead, the model interpolates around the sparse support, leading to point clustering near known estimates or interpolation artifacts that resemble

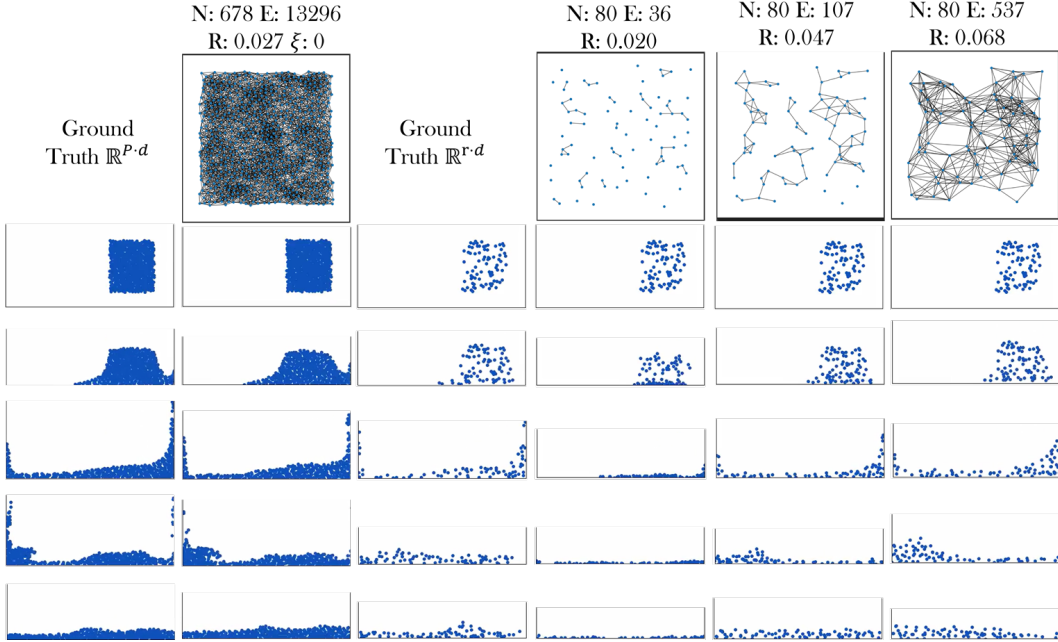


Figure 13: **Water2D at 11% sampling.** All predictions diverge from ground truth. Even at increased radii, rollout MSE remains high. Reduced-space ground truth itself is physically dissimilar to the original system, limiting learnability.

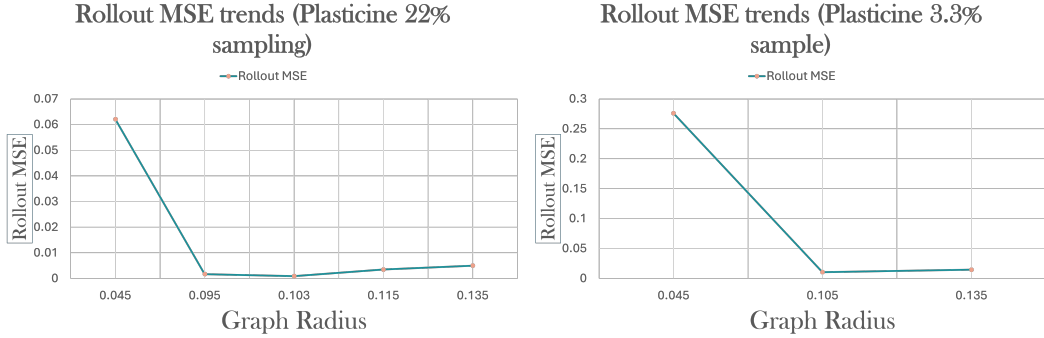


Figure 14: **Plasticine3D: rollout MSE.** Left: 22% sampling shows consistent correlation. Right: At 3.3% sampling, correlation degrades as the reduced graph fails to encode sufficient structure for accurate rollout. At 35%, rollout MSE reduces to 9.2×10^{-4} , while it plateaus at 0.01 at 3.3%

piecewise-linear transitions. These effects arise not due to kernel parameter choices, but due to a fundamental lack of information in the reduced space: the interpolated function no longer reflects a smooth or physically meaningful structure.

This limitation is evident in fig. 15, where we interpolate a 2-million-point Dragon mesh from three different supervision levels: 700 points (0.035%), 20K points (1%), and 60K points (3%). At 700 points, the interpolated output exhibits dense clustering and abrupt discontinuities. The gap between 0.035% and 1% remains substantial. The top-row result makes clear that in the regime of extreme sparsification, the model fails to maintain coherent spatial representations, regardless of neighborhood size or kernel formulation.

This example illustrates the lower bound on sparsity below which the learned representation fails to extrapolate. In such cases, the reduced-space support does not sufficiently reflect the full system’s physical characteristics, making the reconstruction problem ill-posed.

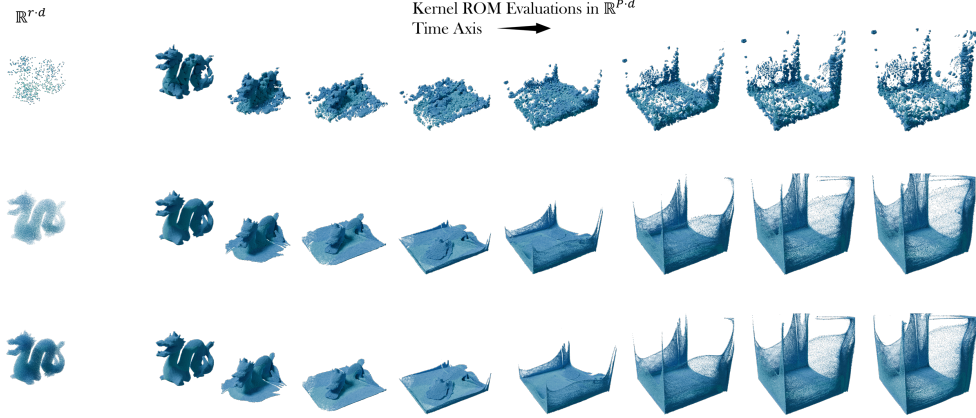


Figure 15: **Degradation under extreme sparsification.** All rows show kernel-ROM interpolation on a 2-million-point Dragon mesh. **Top:** 700 function evaluations (0.035%) lead to clustered and discontinuous outputs. **Middle:** 20K points (1%) **Bottom:** 60K points (3%) produces smoother reconstruction.

J.3 Computational cost of kernel-ROM

We evaluated the computational cost of Kernel-ROM with respect to neighborhood radius, input discretization size, and MLP architecture. Figure 16 (left) shows that, with a fixed input discretization of 3000 points and MLP configuration [128, 256], inference time increases from 3.4 ms to 7.6 ms as the radius grows from 0.009 to 0.035. GPU memory usage also rises significantly, from 122 MB to approximately 4.3 GB. The right panel of Figure 16 shows inference time and memory usage as functions of input size at a fixed radius of 0.015 and the same MLP. Increasing input points from 3000 to 12000 results in inference time increasing from 4.1 ms to 12.8 ms, and GPU memory usage from 414 MB to 1.6 GB.

Figure 17 (left) presents inference time and memory usage for different MLP architectures at fixed radius 0.015 and input size 3000. Increasing the MLP size from [32, 64] to [1024, 1024] raises inference time from 3.8 ms to 8.2 ms and memory usage from 119 MB to 2.1 GB. The right panel shows rollout mean squared error (MSE) decreases with increasing sampling percentage, from 0.045 at 0.035% sampling to 0.0034 at 15% sampling.

These results demonstrate that increasing radius, input discretization, or model size leads to higher computational cost, while higher sampling percentages improve accuracy.

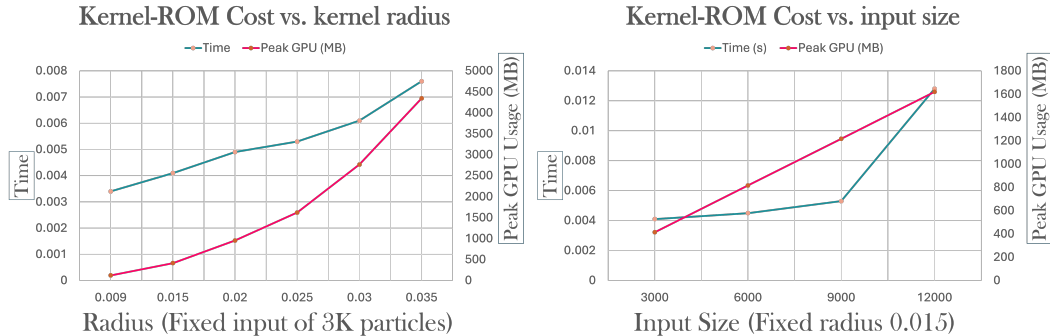


Figure 16: Kernel-ROM inference time and GPU memory usage. Left: Variation with neighborhood radius at fixed input size and MLP configuration. Right: Variation with input discretization size at fixed radius and MLP. These are computed on collision dataset with 84K particles

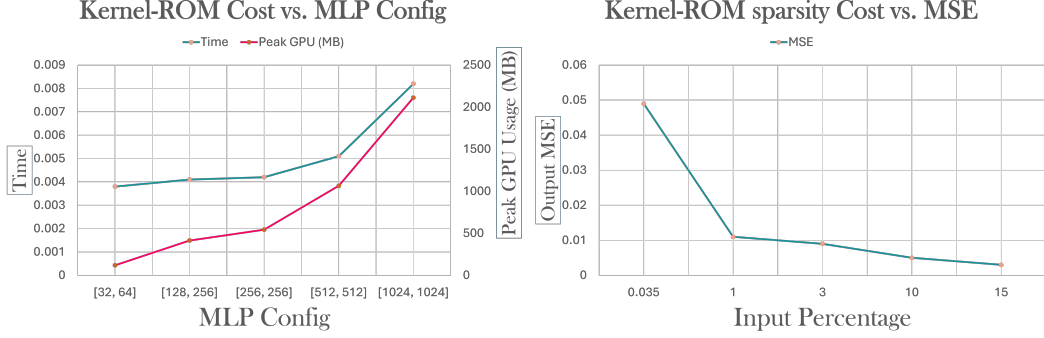


Figure 17: Left: Inference time and memory usage for different MLP sizes at fixed radius and input size. (collision dataset 84K particles) Right: Rollout mean squared error versus sampling percentage for the dragon dataset (2 million particles), providing an empirical lower bound for r

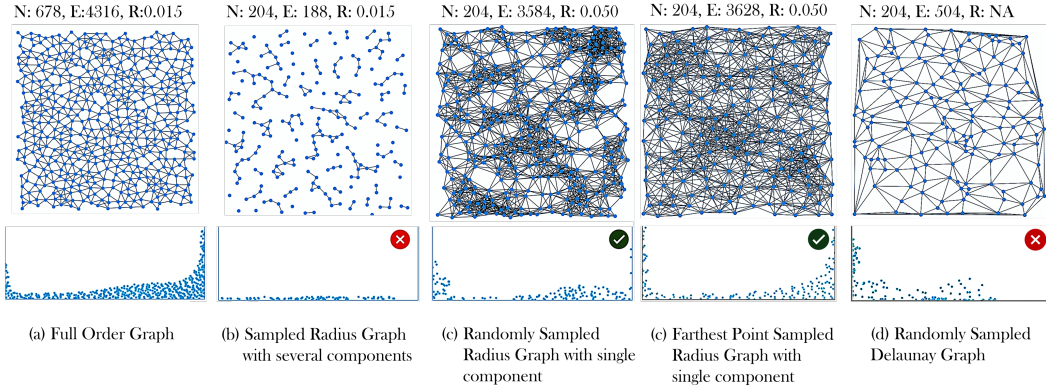


Figure 18: This figure illustrates the critical role of radius-based graphs in maintaining discretization invariance and preserving connectivity in graph structures. Both random sampling and farthest-point sampling produce consistent embeddings due to stable neighborhood definitions, whereas altering the graph construction method breaks the model.

J.4 GNNs as neural operator approximations

We now argue that Graph Neural Networks (GNNs), under a suitable construction, can be interpreted as discretizations of kernel integral operators. In particular, GNNs can be viewed as data-driven approximations to a class of neural operators. However, GNNs are sensitive to input graph topologies, and cannot generalize to arbitrary graph structures defined over a discretization. This can be seen in fig. 18, where the model can generalize to different sampling strategies but not to different graph structures defined over the same sample size.

J.4.1 GNNs as Monte-Carlo estimators

We discuss the following propositions made in [54]. Let $D \subset \mathbb{R}^d$ be a compact domain. For each $x \in D$, let ν_x be a fixed Borel measure on D . We define a kernel integral operator of the form:

$$(\mathcal{K}_\phi v)(x) := \sigma \left(Wv(x) + \int_D \kappa_\phi(x, y)v(y) d\nu_x(y) \right),$$

where $\sigma : \mathbb{R} \rightarrow \mathbb{R}$ is a fixed nonlinearity applied elementwise, $W \in \mathbb{R}^{n \times n}$ is a learned matrix, and $\kappa_\phi : \mathbb{R}^{2(d+1)} \rightarrow \mathbb{R}^{n \times n}$ is a neural network parameterized by ϕ . The arguments to κ_ϕ can include geometric and positional information such as $(x, y, x - y, \|x - y\|)$.

In practice, we do not have access to the continuum D , and instead work with a finite point cloud $\{x_1, \dots, x_K\} \subset D$. We approximate the measure ν_x by an empirical distribution over a neighborhood

$\mathcal{N}(x)$ around each x , typically defined via a radius graph. Then, the integral operator is approximated by a sum:

$$(\mathcal{K}_\phi v)(x) \approx \sigma \left(Wv(x) + \frac{1}{|\mathcal{N}(x)|} \sum_{y \in \mathcal{N}(x)} \kappa_\phi(e(x, y))v(y) \right),$$

where $e(x, y)$ denotes edge features constructed from (x, y) . This yields the following message-passing update rule:

$$v^{t+1}(x) = \sigma \left(Wv^t(x) + \frac{1}{|\mathcal{N}(x)|} \sum_{y \in \mathcal{N}(x)} \kappa_\phi(e(x, y))v^t(y) \right).$$

We interpret this as a discretization of the continuum operator \mathcal{K}_ϕ , where the integral is approximated by local aggregation, and the kernel κ_ϕ is represented by a shared neural network acting on edge features.

The key modeling decision is that κ_ϕ defines a $K \times K$ block kernel matrix, where each entry $\kappa_\phi(x_i, x_j)$ is a matrix in $\mathbb{R}^{n \times n}$. The parameters ϕ are shared across all edge pairs. This sharing ensures that the operator is independent of the number and arrangement of discrete points, so long as the neighborhoods are constructed consistently. Therefore, the learned operator exhibits discretization invariance.

J.4.2 Discretization or resolution?

Figure 19 presents four point clouds of identical size and geometry but with differing point configurations. Despite many non-overlapping locations, the predictions across all four discretizations remain consistent. This visual evidence supports the notion of learned model generalizing across different samplings of the same underlying domain. It is important to distinguish this from resolution, which concerns the density or number of points used to represent the domain. Discretization refers to the specific arrangement of a fixed number of points; resolution, by contrast, changes the number of points altogether. This is a subtle difference.

Implicit handling of self-contact Training data were generated using MPM solvers that handle self-contact implicitly via a background Eulerian grid, applicable to both solids and fluids. As a result, the model implicitly learns self-contact behavior from data. Future work could explore improved sampling strategies in regions prone to self-collision for enhanced resolution.

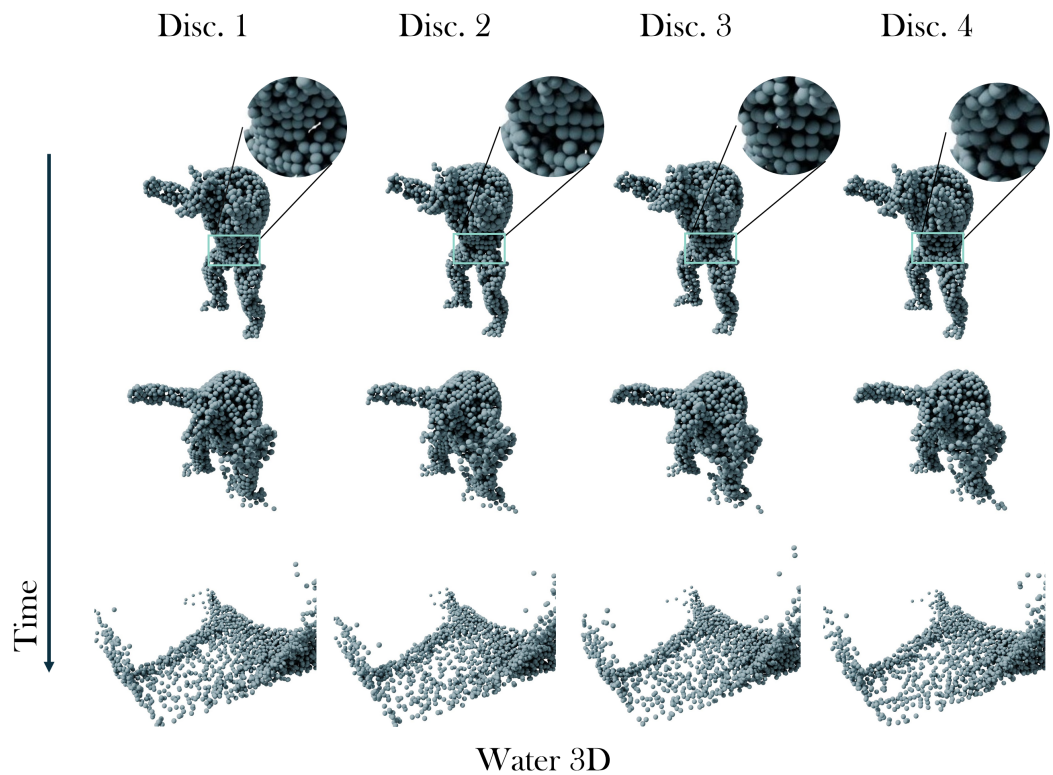


Figure 19: **Discretization invariance on the same geometry.** We construct four different point clouds sampled from the same domain, with equal size but varying locations. On each, we build a radius graph with fixed connectivity radius and apply the same learned GNN layer. Despite the different discrete realizations, the resulting outputs are consistent.